

A born ultramassive white dwarf-hot subdwarf super-Chandrasekhar candidate

Changqing Luo^{1,8}, Jiao Li^{1,8}, Chuanjie Zheng^{1,2,8}, Dongdong Liu³, Zhenwei Li³, Yangping Luo⁴, Péter Németh^{5,6}, Bo Zhang¹, Jianping Xiong¹, Bo Wang³, Song Wang¹, Yu Bai¹, Qingzheng Li^{3,2}, Pei Wang^{1,7}, Zhanwen Han³, Jifeng Liu^{1,2}, Yang Huang^{2,1,9}, Xuefei Chen^{3,9}, Chao Liu^{1,2,9}

¹National Astronomical Observatories, Chinese Academy of Sciences, Beijing 100101, People's Republic of China;

²School of Astronomy and Space Science, University of Chinese Academy of Sciences, Beijing 100049, People's Republic of China;

³Yunnan Observatories, Chinese Academy of Sciences, Kunming 650011, People's Republic of China;

⁴Department of Astronomy, China West Normal University, Nanchong, 637002, People's Republic of China;

⁵Astronomical Institute of the Czech Academy of Sciences, CZ-251 65, Ondřejov, Czech Republic;

⁶Astroserver.org, Fő tér 1, 8533 Malomsok, Hungary;

⁷Institute for Frontiers in Astronomy and Astrophysics, Beijing Normal University, Beijing 102206, China

⁸These authors contributed equally to this work.

⁹Corresponding authors: huangyang@bao.ac.cn; cxf@ynao.ac.cn; liuchao@nao.cas.cn

Although supernovae is a well-known endpoint of an accreting white dwarf, alternative theoretical possibilities has been discussing broadly, such as the accretion-induced collapse (AIC) event as the endpoint of oxygen-neon (ONe) white dwarfs^{1,2}, either accreting up to or merging to exceed the Chandrasekhar limit (the maximum mass of a stable white dwarf). AIC is an important channel to form neutron stars, especially for those unusual systems, which are hardly produced by core-collapse supernovae^{3,4}. However, the observational evidences for this theoretical predicted event and its progenitor are all very limited⁵. In all of the known progenitors, white dwarfs increase in mass by accretion. Here, we report the discovery of an intriguing binary system Lan 11, consisted of a stripped core-helium-burning hot subdwarf and an unseen compact object of 1.08 to 1.35 M_{\odot} . Our binary population synthesis calculations, along with the absence of detection from the deep radio observations of the Five-hundred-meter Aperture Spherical Radio Telescope, strongly suggest that the latter is an ONe white dwarf. The total mass of this binary is 1.67 to 1.92 M_{\odot} , significantly exceeding the Chandrasekhar limit. The reproduction of its evolutionary history indicates that the unique system has undergone two phases of common envelope ejections, implying a born nature of this massive ONe white dwarf rather than an accretion growth from its companion. These results, together with short orbital period of this binary (3.65 hours), suggest that this system will merge in 500 – 540 Myr, largely triggering an AIC event⁶, although the possibility of type Ia supernova cannot be fully ruled out⁷. This finding greatly provides valuable constraints on our understanding of stel-

lar endpoints, whatever leading to an AIC or a supernova.

Main

As a special binary system, unlike the usually discussed binary system with a companion of carbon-oxygen (CO) white dwarf (WD), the final fate of a binary star with a massive oxygen-neon (ONe) white dwarf approaching the Chandrasekhar limit could be either the accretion-induced collapse (AIC)^{1,2} or supernovae type Ia⁷. Depending on the formation channels, AIC has a wide range of delay time, from several tens of Myr to > 10 Gyr, after the birth of its progenitor, and thus can naturally explain the very young radio pulsars found in globular clusters that can not be produced by the core-collapse supernovae given the massive nature of its progenitor⁸. The AIC scenario can also be responsible for explaining a number of unusual neutron stars (NSs), e.g. recycled pulsars with low space velocities due to their low kick velocities⁹, intermediate-mass binary pulsars with short orbital periods¹⁰, the strong magnetic field and slow spin NSs with ultra-light companions ($\leq 0.1 M_{\odot}$) in close orbits^{3,11}, and can even be a promising progenitor of fast radio burst¹² (FRB). The AIC however is still a theoretical prediction without conclusive evidences in observations, although massive efforts are spent to search for both the explosion events and its progenitors^{5,13}.

In this study, we report the discovery of a hot subdwarf–WD binary LAN 11 as a promising AIC progenitor. This system is identified as a nearby (873 pc to the Sun, which is estimated from the *Gaia* parallax measurements^{14,15}), bright (visual magnitude $V = 13.19$) hot subdwarf by the LAMOST low-resolution spectra¹⁶, with large variations in radial velocities revealed by the multi-epoch LAMOST medium-resolution spectroscopic observations. The atmospheric and orbital parameters (listed in Table 1), especially the mass of companion, of this system are then well determined by the high-quality follow-up time-series spectroscopy, from Palomar 200-inch telescope, together with the precise light curves obtained by the Transiting Exoplanet Survey Satellite (TESS). The result shows this is the most massive one among the three detected super-Chandrasekhar hot subdwarf–WD binary systems^{17,18}. It is the first ever found non-accretion binary system with massive WD companion, contrasting with the other two massive white dwarfs found in novae V603 Aql (ref.¹⁹) and RN U Sco (ref.²⁰), which are accreting material from their companions. The heavy mass greater than 1.1 M_{\odot} of the WD indicates that this system will largely end up as an AIC rather than a type Ia supernova (SNe Ia), although the possibility of the latter cannot be totally excluded⁷.

Parameter	Value				
R.A. (J2000)	06:00:30.98				
Decl. (J2000)	+29:08:55.06				
G (mag)	13.079 ± 0.001				
ϖ (mas)	1.146 ± 0.029				
d (pc)	873 ± 22				
μ_α (mas yr ⁻¹)	-1.96 ± 0.03				
μ_δ (mas yr ⁻¹)	-2.91 ± 0.02				
P (min)	219.08880(40)				
RUWE	0.9920				
	Spectroscopic		SED		Light curve
	phase-picked	highest SNR	phase-picked	highest SNR	Adopted interval
$T_{\text{eff}}^{\text{sd}}$ (K)	35840 ± 130	35850 ± 140	35831 ± 128	35839 ± 140	[35710, 35992]
$\log g_{\text{sd}}$ [cm s ⁻²]	5.306 ± 0.020	5.338 ± 0.020	5.302 ± 0.020	5.334 ± 0.020	[5.292, 5.365]
$\log n\text{He}/n\text{H}$	-0.867 ± 0.033	-0.937 ± 0.028	–	–	–
$E(B - V)$ (mag)	–	–	0.16056(89)	0.16069(89)	–
R_{sd} (R_\odot)	–	–	0.275 ± 0.007		[0.265, 0.282]
T_0 (BJD-2459477)	0.82316(46)		–	–	[0.82161, 0.82195]
K_{sd} (km s ⁻¹)	249.8 ± 2.1		–	–	[247.6, 252.2]
RV_γ (km s ⁻¹)	-4.8 ± 1.5		–	–	–
$\sqrt{e} \cos \omega$	-0.148 ± 0.035		–	–	[-0.070, 0.015]
$\sqrt{e} \sin \omega$	0.039 ± 0.052		–	–	[-0.023, 0.038]
i (°)	–	–	–	–	[45.4, 55.5]
M_{sd} (M_\odot)	–	–	–	–	[0.524, 0.651]
M_{comp} (M_\odot)	–	–	–	–	[1.0751, 1.353]
M_{all} (M_\odot)	–	–	–	–	[1.673, 1.922]
q	–	–	–	–	[1.73, 2.48]
L_{sd} (L_\odot)	–	–	–	–	[104.5, 118.4]
a (R_\odot)	–	–	–	–	[1.423, 1.491]
$R_{\text{sd}}^{\text{Roche-lobe}}$ (R_\odot)	–	–	–	–	[0.445, 0.482]
$R_{\text{comp}}^{\text{Roche-lobe}}$ (R_\odot)	–	–	–	–	[0.612, 0.681]

Table 1 – Astrometric, stellar, and orbital parameters for Lan 11. Astrometric parameters are taken from *Gaia* DR3¹⁴. The reported parallax has been corrected for a zero-point of -0.033 mas¹⁵. The stellar parameters are mainly determined from the spectral template matching and the SED fitting. The orbital parameters are constrained from the radial velocity curve fitting and TESS light curve modeling by using `ellc` and `PHOEBE` independently. Quantities shown are the right ascension RA, declination DEC, *Gaia* G -band magnitude, parallax ϖ , distance d , proper motions in the directions of right ascension μ_α , and declination μ_δ , the orbital period P , the Renormalised Unit Weight Error RUWE, the hot subwarf effective temperature $T_{\text{eff}}^{\text{sd}}$, surface gravity $\log g_{\text{sd}}$, helium abundance $\log n\text{He}/n\text{H}$, extinction $E(B - V)$, radius R_{sd} , the superior conjunction time T_0 , the radial velocity semi-amplitude of the hot subdwarf K_{sd} , the systemic velocity of the binary RV_γ , the eccentricity e , the longitude of periastron ω , the orbital inclination i , the hot subdwarf star mass M_{sd} , the companion star mass M_{comp} , the total mass of the binary M_{all} , the mass ratio q , luminosity L_{sd} , the orbital separation a , the effective Roche-lobe radii of the hot subdwarf star $R_{\text{sd}}^{\text{Roche-lobe}}$ and the companion star $R_{\text{comp}}^{\text{Roche-lobe}}$.

Results

Light curve. Lan 11 was observed by TESS in Sectors 43, 44, and 45 with 2 minutes cadences. The whole data, including 50,447 data points, covers a baseline of around 76.5 days. A significant peak at 109.54440(20) min is seen in the periodogram by performing Lomb-Scargle analysis to the TESS light curve (see Supplementary Figure 3). The phase-folded light curve, assuming a period of twice of the peak value found in the periodogram, is shown in Figure 1(a). Clearly, a small but significant effect of Doppler beaming is detected between adjacent maxima, with a height difference around 0.2%, suggesting an orbital period of 219.08880(40) min (corresponding to the sec-

ond harmonic peak in Supplementary Figure 3). The light curve also shows obvious ellipsoidal variations of a semi-amplitude of 1% level, implying significant tidal force from a compact companion.

Radial velocity curve and stellar parameters Between October 2017 and February 2021, 34 exposures medium-resolution spectra with $R \sim 7500$ are collected for Lan 11 by LAMOST (see Supplementary Table 1). The radial velocities are measured from the $H\alpha$ lines by using the LAMOST spectra from red arm (see Methods). The phase-folded radial velocity curve, by adopting the orbital period obtained above, is presented in Figure 1(b), showing a significant sinusoid-like mo-

tions with semi-amplitude larger than 200 km s^{-1} . Due to the shallow limiting magnitude of LAMOST medium-resolution observations, the quality, in sense of both time resolution (longer than 10 minutes) and measurement errors (typically 10 km s^{-1}), of the radial velocity curve suffers from large uncertainties. Time-series spectra are therefore collected for Lan 11 by using the Double-Beam Spectrograph (DBSP) equipped in the Palomar 200-inch telescope during February 19, 2022 (see Supplementary Table 2). In total, 28 spectra with a typical spectral signal-to-noise ratio (SNR) greater than 80 are obtained, covering the full orbital phase of Lan 11. The radial velocities are then precisely determined by performing cross-correlation of each collected spectrum to the model template (see Methods for details). The phase-folded radial velocity curve from DBSP, with a typical measurement error of 1.3 km s^{-1} , is also shown in Figure 1(b).

The canonical single-line binary radial orbit model is adopted to fit this radial velocity curve, by fixing the period to the solution of light curve (see above). The best-fit model, shown in Figure 1(b), reveals a large radial semi-amplitude of $K_{\text{sd}} = 249.8 \pm 2.1 \text{ km s}^{-1}$ of this hot subdwarf. The mass function of the unseen companion is then determined by the light curve and radial orbital solutions:

$$\begin{aligned} f_{\text{comp}} &= \frac{M_{\text{comp}}^3 \sin^3 i}{(M_{\text{sd}} + M_{\text{comp}})^2} \\ &= \frac{PK_{\text{sd}}^3}{2\pi G} = 0.2456_{-0.0061}^{+0.0063}. \end{aligned} \quad (1)$$

The systemic velocity from the radial orbital solution, together with the positions, proper motions and distances measured from *Gaia*¹⁴, shows that this system is rotating the Galactic center with a speed of $237.80_{-0.20}^{+0.18} \text{ km s}^{-1}$, implying its nature of the thin disk population (Methods).

By performing spectral fits to either the single-epoch DBSP spectrum with the highest signal-to-noise ratio (SNR) or four phase-picked high-SNR DBSP spectra with the XTGRID tool²¹ (Methods), the visible component is found to be an sdOB with $T_{\text{eff}}^{\text{sd}}$ around 35,800 K (with a typical uncertainty of 140 K), $\log g_{\text{sd}}$ ranging from 5.29 to 5.36 and a helium-to-hydrogen ratio $\log n\text{He}/n\text{H}$ between -0.83 and -0.97 (see Table 1). As shown in Figure 2(a) and Supplementary Figure 5, the best-fit model spectrum agrees very well with the observed ones from DBSP. The obtained parameters are also consistent with previous estimates from LAMOST low-resolution spectra¹⁶.

By combing with the distance estimate from *Gaia* parallax, we determined the stellar radius of the hot subdwarf from its spectral energy distribution (SED) composed of the multi-band photometry. The values of $T_{\text{eff}}^{\text{sd}}$ and $\log g_{\text{sd}}$, as well as uncertainties, yielded from above spectral fits are taken as the priors during the SED fitting (see Methods). Figure 2(b) clearly shows that the contribution of a single hot subdwarf with $T_{\text{eff}}^{\text{sd}}$ and $\log g_{\text{sd}}$ listed in Table 1 is in excellent agreement with the observed SED, implying negligible contributions from the unseen companion. The resulting reddening of $E(B - V) = 0.161 \pm 0.001$ is very close to the value of 0.168 reported by the 3D dust map²². We finally obtained the radius of $R_{\text{sd}} = 0.275 \pm 0.007 R_{\odot}$ for the hot subdwarf.

Discussion

The nature of the unseen companion. The ultra-high precision light curve from TESS has enabled us to infer the mass of the unseen companion star, given its modulations on the light curve from the tidal force. We then modeled the light curve of Lan 11 by two independent advanced software packages: `e11c`²³ and `PHOEBE`²⁴ (Methods). The detail setups, including priors of input parameters, are described in Methods. The well-constrained parameters, including the inclination angle (i), the eccentricity (e), and the longitude of periastron (ω), are consistent with each other from the light curve solutions of both `e11c` and `PHOEBE`. By combing the solutions from both packages, we obtain an inclination angle of $45.4 - 55.5$ degree and a companion mass of $1.08 - 1.35 M_{\odot}$. As suggested by our binary population synthesis (BPS) simulation (Methods), this unseen object has more than 85% probability to be a WD with an ONe core, according to its massive nature (ref.²⁵). The probability that the massive companion is a neutron star (NS) is only around 5%, meaning that this channel can not be fully ruled out. The probability to be a NS is much lower than that of an ONe WD. This is due to that the high-mass (largely greater than $12 M_{\odot}$, ref.²⁶) of neutron star’s progenitor is not preferred by both the initial mass function and the extremely mass-ratio of the primordial binary ($q \geq 4$; see Figure 3(b)). Moreover, the companion nature of a WD (rather than a NS) is supported by the non-detection from the deep radio observations (Methods) of the Five-hundred-meter Aperture Spherical radio Telescope (FAST).

The past and future of Lan 11 This system, with a total mass of $1.67 - 1.92 M_{\odot}$, is the most massive super-Chandrasekhar hot subdwarf–WD (suggested by our BPS simulation) binary system ever found (see Figure 3(a)), which is very interesting and unique system compared to other super/sub-Chandrasekhar systems^{17,19,20,27,28,18,29,30}. With the observational constraints, we investigated the possible formation pathway (see Figure 3(b)) of this system by performing numerical simulations under the assumptions of solar metallicity and “Dutch” mass-loss scheme³¹ with an efficiency of $\eta = 0.50$ (Methods). The nature of short period suggests that Lan 11 is formed through two phases of common envelope (CE) ejection processes. The primordial binary is initially consisted of a $\sim 7 - 12 M_{\odot}$ intermediate-massive star and a $\sim 2 - 3 M_{\odot}$ main-sequence (MS) star. The more massive one evolves first and fills its Roche lobe at the giant branch (RGB/AGB) with a He-burning core about $2.0 - 2.5 M_{\odot}$. The binary then enters into the first CE phase given the large mass-ratio³². The envelope is ejected due to the low binding energy, a binary consisted of a He star with mass around $2.0 - 2.5 M_{\odot}$ and an evolved companion star is then formed. The radius of the He star can further expand to a few hundreds solar radius so as to fill its Roche lobe that leads to the so-called case BB mass transfer^{33,34}. After this mass transfer, a massive ONe WD around $1.2 M_{\odot}$ (see Figure 2 of ref.³⁴) and a companion star with mass around $2.6 - 3.2 M_{\odot}$ are then left. This system will enter the second CE phase when the companion star fills its Roche lobe. After the ejection of the second CE, the Lan 11-like system consisted of a sdOB star and a massive ONe WD, is formed. Under the aforemen-

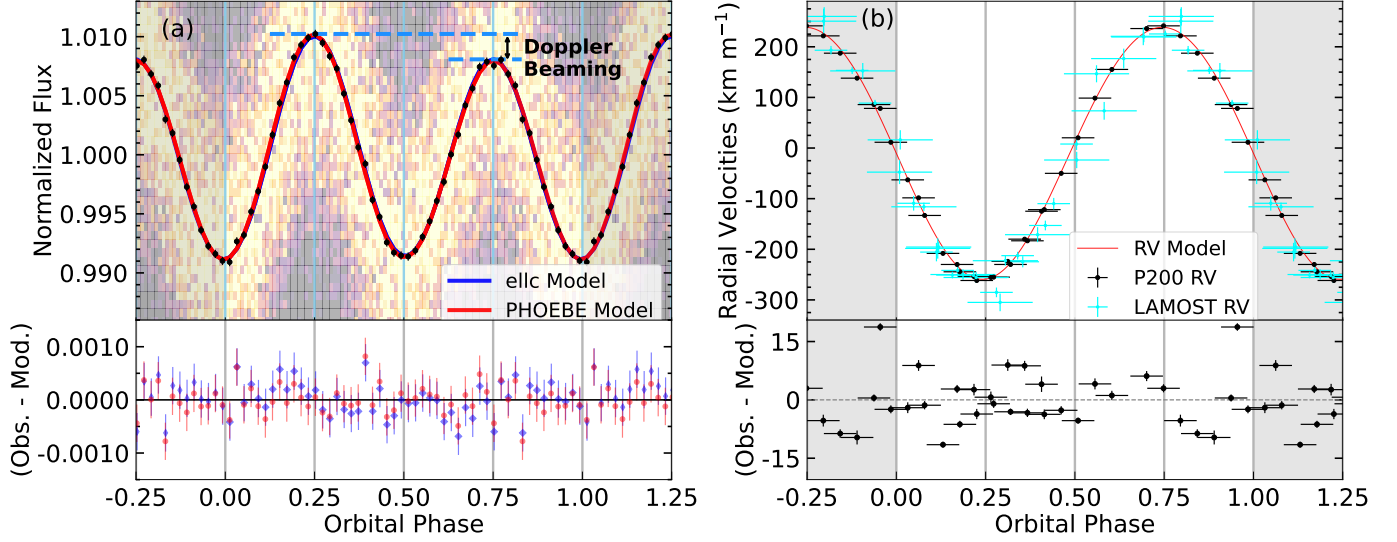


Figure 1 – Phased data for Lan 11. (a): Phase folded light curve and its fitting residuals. The original TESS data points are shown in the background density plot. Black dots represent the binned data by each one-fifty phase for the light curve fit. The error bars show the 1σ uncertainty for each binned data. The different height between adjacent maxima is mainly caused by the Doppler boosting. The red and blue solid lines represent, respectively, the best-fit models found by `e11c` (blue) and `PHOEBE` (red) with priors on atmospheric parameters from the highest SNR spectrum. The lower part of this panel shows the model residuals. (b): Phase folded radial velocity curve and its fitting residuals. The individual radial velocity measurements are shown as black dot (from P200) and cyan dot (from LAMOST), respectively, as well as their 1σ uncertainties and exposure duration. The red line represents the best-fit model for the radial velocity curve obtained from P200, with the fitting residuals shown in the lower part.

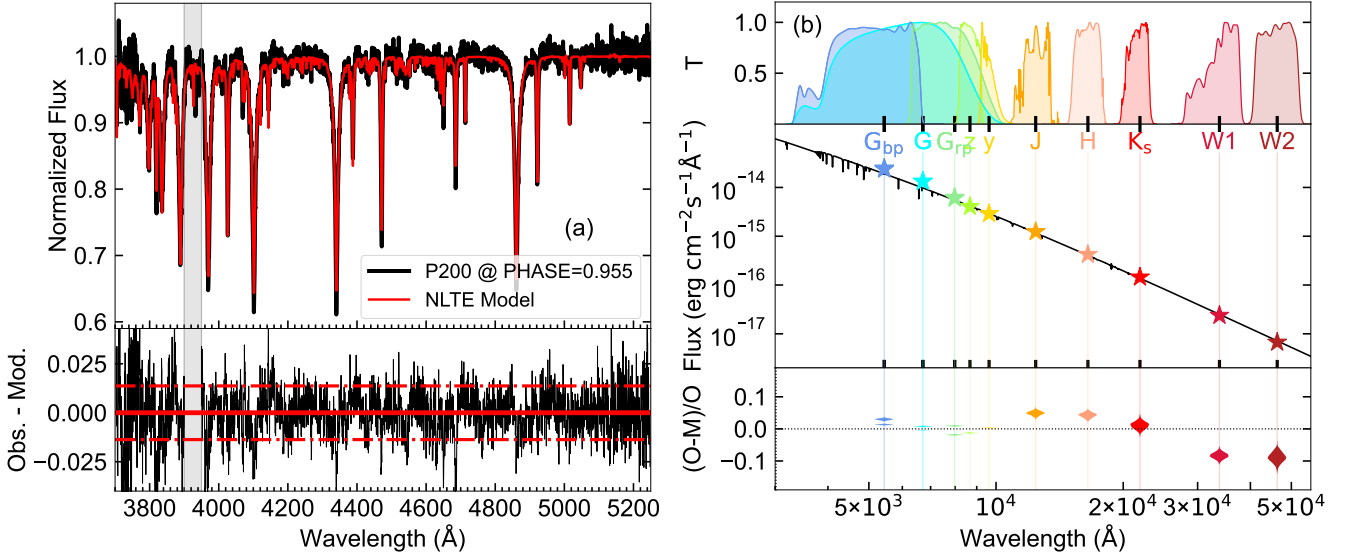


Figure 2 – The estimates of the stellar parameters of hot subdwarf. (a): The normalized highest SNR DBSP spectrum of Lan 11 is shown as black line, together with the best-fit synthetic spectrum ($T_{\text{eff}} = 35,850$ K, $\log g = 5.338$ and $\log n\text{He}/n\text{H} = -0.937$) shown in red. The fitting residuals are shown in the lower part of the panel. The dotted line represents the standard deviation of the residuals. The shadow vertical band represents the Ca K line region ($3850 - 3885\text{\AA}$) that is masked (avoid the influence of interstellar medium absorption) during spectral fits. (b): The broadband spectral energy distribution of Lan 11. Stars represent the observed flux from the *Gaia* EDR3 G_{bp} -, G - and G_{rp} -bands, PanSTARRS z - and y -bands, 2MASS J -, H - and K_s -bands, and ALLWISE W_1 - W_2 bands. The transmission curves for these broadband filters are displayed in the top panel and normalised at the maximum. The black curve is the best-fit ‘tmap’ model spectrum for the hot subdwarf. The relative fitting residual, defined as $(O-M)/O$, is shown in the lower panel. Vertical range of these violin symbols represent the photometric uncertainties.

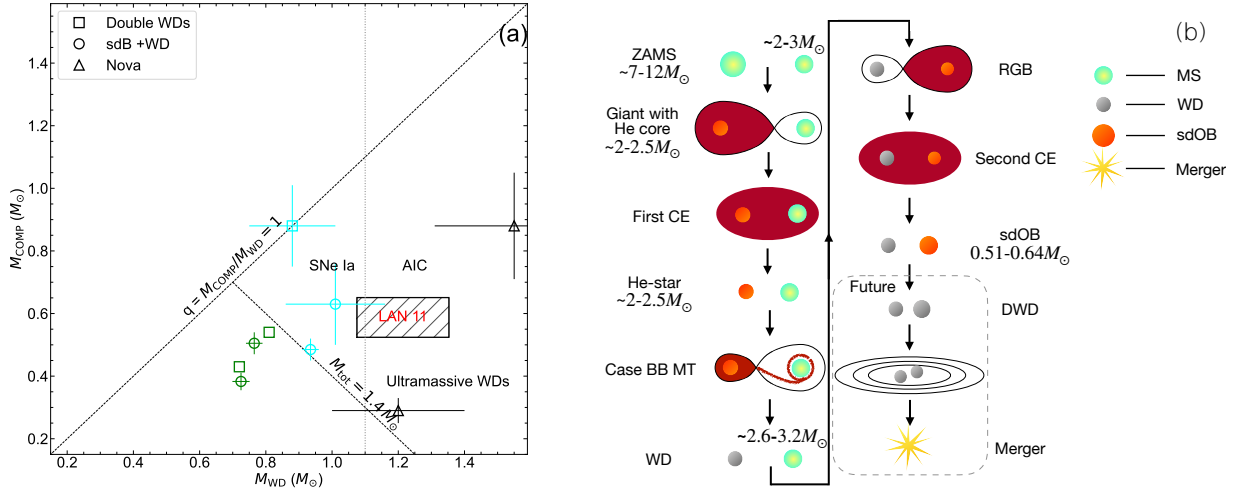


Figure 3 – The mass-mass diagram and the carton of the evolutionary history of Lan 11. (a): Mass-mass diagram of the binary systems that are potential candidates of type Ia supernovae (SNe Ia) and accretion-induced collapse (AIC). Symbols of square, circle and triangle represent the double white dwarfs (WDs), the hot subdwarf (sdB)–WD and the classical or recurrent nova consisted by a WD plus a non-degenerate companion. The green and cyan symbols mark the known sub-Chandrasekhar and super-Chandrasekhar candidates of SNe Ia. The dotted line indicates the definition of ultramassive WD with mass greater than $1.1 M_{\odot}$. Lan 11 is the only sdB-WD system that could end up with an AIC event. **(b):** The past and future of Lan 11. The binary may experience two CE ejection phases and a case BB mass transfer phase to produce Lan 11.

tioned conditions, our simulations successfully reproduce the Lan 11 system with the mass of sdOB star ranging from 0.51 to $0.64 M_{\odot}$ (similar to the observed interval for Lan 11). SdOB star in such a mass range can cross the observed intervals of Lan 11 very well in $T_{\text{eff}}-\log g$ diagram (see Supplementary Figure 11). According to our simulations, this sdOB star will soon (after few ten Myrs) evolve to white dwarf, and this binary will become a double-degenerate system. Due to gravitational wave radiation, this double-degenerate system will eventually merge in 500 to 540 Myr. In a widely accepted scenario, the super-Chandrasekhar nature and the presence of a massive ONe WD in this binary strongly suggest that the final violent merger will trigger the electron-capture reactions involving ^{20}Ne and ^{24}Mg , then the ONe WD collapses to a NS – the so-called AIC process (refs.^{1,2}). This system may also explode as a type Ia supernova, if a detonation can be triggered in ONe WD matter⁷. This may be possible but has not yet been proven to work³⁵.

Methods

Observations and data reduction. Lan 11 (TIC 79323477) was visited by TESS on September 15, 2021 to December 02, 2021 (Sectors 43-45), with a cadence of two-minute. The data was downloaded from the Mikulski Archive of Space Telescopes (MAST, <https://mast.stsci.edu/portal/Mashup/Clients/Mast/Portal.html>), which was properly reduced and calibrated by the TESS Science Processing Operations Center (SPOC) pipeline. We adopted the Pre-search Data Conditioning Simple Aperture Photometry (PDCSAP) flux data to construct our light curve. We note that the PDCSAP performed simple aperture photometry by removing the instrumental trends and the aperture contributions

of neighboring stars identified in a pre-search data condition (PDC). The later function in PDCSAP is particularly important for Lan 11 since the existences of two bright nearby stars with Gaia RP-band magnitudes of 13.97 and 14.35 just around $28''$ away. We carefully check the two neighbors in Zwicky Transient Facility (ZTF) database³⁶ and find their magnitudes are almost stable during 1500 days observations. To further check the robustness of the contamination corrections from neighboring stars, we compare phase-folded light curves (with period taken from Table 1) in each sector (see Supplementary Figure 2) and find they are consistent with each other very well. Moreover, the ZTF g - and r -band phase-folded light curves of Lan 11 are also in excellent agreement with that of TESS within measurement errors. To this degree, the light curve amplitude should be properly corrected by the PDCSAP algorithm.

As shown in Supplementary Table 1, a total of 34 medium resolution ($R \sim 7500$) spectra were taken by LAMOST during October 2017 and February 2021. The typical exposure time is from 10 to 20 min, yielding spectra with typical SNR around 5 in the blue arm and 10 in the red arm. The high-quality time-series optical spectra were obtained by DBSP installed on Palomar 200-inch telescope. In total, twenty-eight exposures of 600s were taken with a slit width of $0.''5$ on February 19, 2022 (see Supplementary Table 2). Unfortunately, the red arc lamp is broken during that night. But the spectra at blue arm are well-observed with three exposures of FeAr arc taken during the scientific observations. Given a resolving power of 2500, the obtained spectra are sufficient to derive accurate radial velocities, as well as the determinations of stellar parameters for Lan 11. The standard data reductions, including bias subtraction, flat correction, cosmic ray removal, one-dimensional-spectrum ex-

traction, wavelength calibration, and flux calibration were performed by using a Python package `pyexspec` developed ourselves.

FAST observation and data reduction. We performed a total of 2,300s of targeted exceptionally sensitive radio follow-up observation for Lan 11 using the Five-hundred-meter Aperture Spherical radio Telescope (FAST) on Dec 05, 2022. Note the first 1 min and the last 1 min were used for signal injection and polarization calibration. The Observation taken at FAST are using the center beam of the 19-beams L-band receiver, that the frequency range is from 1.05 to 1.45 GHz with an averaged system temperature around 25 K (ref.³⁷). Observation data is recorded in pulsar search mode, stored in PSRFITS format³⁸. Two types of data processing were performed for this observation: dedicated and blind search and single pulse search.

Dedicated and blind search. Due to model dependence of the Galactic electron density model NE2001 (ref.^{39,40}) and for the sake of robustness, we created de-dispersed time series for each pseudo-pointing over a wide range of dispersion measures (DMs), from 0 to 2,000 pc cm⁻³, which is a factor of 7 larger than the Galactic maximum DM = 272.56 pc cm⁻³ that models predicted in this line of sight. For each of the trial DMs, we searched for a periodical signal and first two order acceleration in the power spectrum based on the PRESTO pipeline^{41,42}. We checked all the pulsar candidates with SNR greater than 6 pulse-by-pulse and removed the narrow-band radio frequency interferences (RFIs).

Both the periodical radio pulsations and single-pulse blind searches were performed for each observing epoch, but resulted in non-detections for all searches. We calibrated the noise level of the baseline, and then measured the amount of pulsed flux above the baseline, giving a 6 σ upper limit of flux density measurement of $41 \pm 3 \mu\text{Jy}$ for persistent radio pulsations (assuming a pulse duty cycle of 0.05 to 0.3).

Single pulse search The above search strategy was continued to apply to de-disperse the time series for single pulse search. The soft packages PRESTO and HEIMDALL (<https://sourceforge.net/p/heimdall-astro/wiki/Home/>) are adopted. A zero-DM matched filter was applied to mitigate RFI in the blind search. All of the possible pulse-candidates were plotted, then be checked as RFIs by manual eyes one-by-one. No pulsed radio emission with dispersive signature was detected with SNR > 6. The upper limit of pulsed radio emission is $\sim 0.15 \text{ Jy ms}$ by assuming a 1 ms wide burst in terms of integrated flux.

Stellar properties and orbital parameters of Lan 11 We present an overview of the estimates of stellar properties and orbital parameters in Supplementary Figure 1, by using the observation data described above. The estimates include period determination, radial velocity (RV) curve fitting, spectral template matching, spectral energy distribution (SED) fitting, and light curve fitting, which will be detailedly described in the following subsections one-by-one. The main results are summarized in Table 1.

Period determination We performed a Lomb-Scargle periodogram for the TESS light curve using the function of `LombScargle` implemented in `Astropy`⁴³. To search realistic periodicity, the frequency range is set from $\frac{1}{T_{\text{base}}}$ to $\frac{1}{2\Delta T}$ with

a step of $0.2 \times \frac{1}{T_{\text{base}}}$, where $T_{\text{base}} = 76.457$ days and $\Delta T = 120$ s are the total observation duration (three sectors here) and the cadence of TESS light curve, respectively. The periodogram shows a significant peak around 110 min (see Supplementary Figure 3). We apply a Gaussian fit to the periodogram and find the peak value of 109.54440(20) min. Phase-folded light curve to twice the peak value shows a clear Doppler beaming effect in the consecutive maxima with a height difference around 0.2% (see Figure 1(a)), which is consistent with the amplitude of the radial velocity curve (see Figure 1(b)). This result suggests that the orbital period of Lan 11 is twice of the peak value, i.e. $P = 219.08880(40)$ min, which is also clearly detected in the periodogram as the second harmonic (see Supplementary Figure 3). The light curve of Lan 11 shows a semi-amplitude of 1% ellipsoidal variations, which is caused by the strong tidal force of its companion.

Radial velocity curve and fitting Lan 11 was first identified as a variable stars from its radial velocity measured from the LAMOST medium resolution survey. However, due to the short wavelength coverage, low spectral SNR, and long exposure time (10-20 min), the high-quality time-series spectra were further collected using DBSP equipped in P200 telescope.

Radial velocity from LAMOST We measured the radial velocity from H α lines in the red arm spectra by fitting a Gaussian function (for the absorption line) plus a second-order polynomial (for the continuum) with the IDL software package `mpfit`. Other lines were not used for radial velocities either due to the low SNR in the blue arm or the weak lines in the red range. The typical uncertainties of the measurements are 10 km s^{-1} . We applied a simple sinusoidal function to fit the radial velocity curve by fixing the orbital period found from the TESS light curve. The semi-amplitude found by the fitting is $251.15 \pm 10.00 \text{ km s}^{-1}$.

Radial velocity of DBSP spectra The radial velocities were measured from the spectra between 3750 and 5200 Å obtained from P200 DBSP by using the cross-correlation function (CCF) method with a grid of synthetic spectra for subdwarfs. The grid includes 96 synthetic spectra with effective temperature ranging from 10,000 to 65,000 K (in a step of 5000 K for $T_{\text{eff}} \leq 45,000$ K and a hottest template with $T_{\text{eff}} = 65,000$ K), surface gravity covering 4.5 to 6.5 (in a step of 1.0 dex) and four representative chemical abundances. Please refer to ref.⁴⁴ for details. A Gaussian kernel with FWHM $\sim 1.8 \text{ \AA}$ was used to degrade the synthetic spectra to fit the DBSP resolution ($R \sim 2500$). We then derive the radial velocity for each DBSP spectrum by using the CCF method developed in ref.⁴⁵, with the above degraded synthetic spectra and a radial velocity grid of -500 to 500 km s^{-1} in a step of 5 km s^{-1} . The uncertainties of the measured radial velocities were evaluated using the Monte Carlo (MC) method by sampling the spectra 100 times using the individual flux error of each pixel. The whole measurements were realized by using the radial velocity module in `Laspec`⁴⁶. The results are presented in Supplementary Table 1.

Radial velocity curve fitting By fixing the orbital period $P = 219.08880$ min obtained from the TESS light curve, we derived the orbital parameters of the Lan 11 by fitting its radial velocity curve measured from DBSP spectra using the Markov Chain Monte Carlo (MCMC) approach. The likelihood of the

parameters are adopted such that

$$\begin{aligned} \ln[\mathcal{L}(\theta_v | v)] &\propto \ln[\mathcal{L}(v | \theta_v)] \\ &= -\frac{1}{2} \sum_{i=1}^N \frac{[v_i - v(\theta_v, t_i)]^2}{\sigma_{v_i}^2 + s^2} \\ &\quad - \frac{1}{2} \sum_{i=1}^N \ln[2\pi(\sigma_{v_i}^2 + s^2)], \end{aligned} \quad (2)$$

where v_i and σ_{v_i} are the radial velocities and their measurement errors, respectively, measured from the DBSP spectra, and $\theta_v = (P, T_0, K_{sd}, v_\gamma, \sqrt{e} \cos \omega, \sqrt{e} \sin \omega)$ are the orbital parameters. K_{sd} , e , ω , and v_γ are the radial velocity semi-amplitude, eccentricity, longitude of periastron, and the systematic radial velocity. $v(\theta_v, t_i)$ represents the Kepler orbital radial velocity at epoch t_i with orbital parameters θ_v , calculated by the function `rv_drive` implemented in the python package `radvel`⁴⁷. s is an additional ‘‘jitter’’ variance which may absorb all kinds of modeling errors such as errors of the instrument, wavelength calibration, and even the radial velocity model. We note that the value of $v(\theta_v, t_i)$ is calculated by considering the exposure duration (10 min, about 5% of the period):

$$v(\theta_v, t_i) = \frac{1}{10 \text{ min}} \int_{t_i - 5 \text{ min}}^{t_i + 5 \text{ min}} v(\theta_v, t) dt, \quad (3)$$

where t_i is the middle time of each exposure. The fitting results are listed in Table 1, the posterior distributions of these orbital parameters are shown in Supplementary Figure 7. The semi-amplitude of the radial velocity curve from DBSP spectra is $K_{sd} = 249.8 \pm 2.1 \text{ km s}^{-1}$, which is consistent with the result found from LAMOST radial velocity measurements. A small eccentricity $e = 0.02 \pm 0.01$ is found after the fitting procedure. We note this is only an upper limit, given the 10 min exposure duration and sparse sampling of P200 spectroscopic observations. The eccentricity will be well constrained by the high-precision and well-sampling TESS light curve in the later analysis.

Kinematics of Lan 11 We determined the 3D velocity of Lan 11 by using the positions, distance, proper motions from *Gaia*, and the systemic velocity from the radial velocity curve fitting. During the calculation, the Sun is placed at $(R, Z) = (8.178, 0.025) \text{ kpc}$ (refs.^{48,49}) with peculiar velocities with respect to the Local Standard of Rest $(U_\odot, V_\odot, W_\odot) = (7.01, 10.13, 4.95) \text{ km s}^{-1}$ (ref.⁵⁰). The circular velocity at the solar position was assumed as $V_c(R_0) = 234.04 \text{ km s}^{-1}$ (ref.⁵¹). The resulting 3D velocity of Lan 11 is $(V_R, V_\phi, V_Z) = (-11.90^{+1.58}_{-1.47}, 237.80^{+0.18}_{-0.18}, -8.31^{+0.37}_{-0.34}) \text{ km s}^{-1}$. The large azimuthal velocity implies that Lan 11 is a thin disk star. The Galactic orbits (see Supplementary Figure 4) for Lan 11 were further calculated by using the python package `Gala`⁵² with the potential setting to `MilkyWayPotential`⁵³. The orbits show that the eccentricity e and the maximum distance above the Galactic plane z_{max} are 0.06 and 0.16 kpc, respectively. This is again evident that Lan 11 belongs to the thin disk population.

Spectral template matching with XTGRID The accurate determinations of atmospheric parameters of hot subdwarf in such a close binary is challenging. The choices of proper spectra should consider 1) the quality (SNR), 2) the phase (avoid

effects of geometric distortions from the tidal force of the unseen object) and 3) the number of spectra (avoid line broadening from Doppler shift corrections). Doing so, two choices of spectra are adopted to derive reliable atmospheric parameters of Lan 11. First, the DBSP spectrum with the highest SNR (> 135) was chosen to meet requirements 1) and 3). Second, four high quality (SNR > 100) DBSP spectra at different phases (see Supplementary Table 2) were chosen to meet requirements 1) and 2). The atmospheric parameters of Lan 11 were then measured by matching either the highest SNR DBSP spectrum or four phase-picked high-SNR DBSP spectra with the synthetic spectra using a steepest-descent iterative spectral analysis implemented in the XTGRID code²¹. The synthetic spectra were generated by the Non-Local Thermodynamic Equilibrium (NLTE) atmospheric models of TLUSTY (v207) and SYNSPEC (v53)^{54,55}. By starting with an initial guess, XTGRID applies a steepest-descent χ^2 minimization, based on successive approximations, until the parameters converge to the best solution. The procedure calculates new models on the fly and adjusts the model parameters and atomic data inputs to precisely link the variations in the theoretical atmospheric structure to the observable emergent spectrum. We applied H, He, C, N, O, Mg, and Si opacities in the model calculations and, in addition, S in the spectral synthesis. All comparisons were done globally, using the observed spectra with the wavelength range of 3750 – 5200 Å (with Ca K line masked out to avoid the influence of interstellar medium absorption) and a piecewise normalization of the model to the observation. During this process, the effective temperature, surface gravity, projected rotation velocity, and chemical abundances are adjusted independently to minimize the global χ^2 . As an example, the best-fit model for the highest SNR DBSP spectrum is shown as the red line in Figure 2 (a). More comprehensive comparisons for the individual Balmer and helium lines are shown in Supplementary Figures 5–6. During error calculations, new models are calculated radially outward from the best-fit point until the confidence limit is reached. The best-fit parameters for the highest SNR spectrum and four phase-picked high-SNR spectra are presented in Table 1. By combining the two groups of estimates, the 1σ interval is [35,710, 35,990] K for $T_{\text{eff}}^{\text{sd}}$, [5.29, 5.36] for $\log g_{\text{sd}}$, and [−0.97, −0.83] for $\log n\text{He}/n\text{H}$.

Spectral energy distribution fitting We used the spectral energy distribution (SED) fitting method to determine the radius, luminosity and extinction of Lan 11. A python program `SPEEDYFIT`¹ was adopted to determine the stellar parameters, as well as their uncertainties, by using the MCMC approach. During the fitting, photometric fluxes and their uncertainties from *Gaia* EDR3, PanSTARRS, 2MASS, and ALLWISE and parallax measurements from *Gaia* EDR3, as well as Gaussian priors on the effective temperature and $\log g$ from the spectroscopic solutions, were applied. The synthetic spectral model grid for hot subdwarf stars was generated by ‘‘TMAP’’, which is equipped by `SPEEDYFIT`. The posterior probability distributions of these parameters are shown in Supplementary Figure 8. The best-fitted SED by a single hot subdwarf agrees very well with the observed multi-band photometry (see Figure 2(b)).

¹<https://speedyfit.readthedocs.io/en/stable/index.html>

This result suggests the contribution to the observed SED from the unseen companion is negligible, implying a compact nature of the dark companion. The resulting parameters are listed in Table 1.

Light curve fitting In principle, the ellipsoidal light curve of such a close binary is mainly determined by the orbital parameters and stellar properties ($T_{\text{eff}}^{\text{sd}}$, $\log g_{\text{sd}}$ and R_{sd}) of the visible star. The mass function of Lan 11 has been determined from the RV curve fitting, and the stellar properties are well constrained from the spectral template matching and the SED fitting. With these known parameters as priors (see Supplementary Figure 1), the binary inclination angle i and eccentricity e can be well extracted from the light curve. The TESS light curve is modelled with two popular packages: `ellc`²³ and `PHOEBE`²⁴, respectively. Before modeling, the TESS light curve from Sectors 43-45 is normalized by using a python package `LightKurve`⁵⁶ and significant outliers were removed by a 3σ -clipping procedure. The normalized light curve was then phase-folded and further divided into 50 equal bins. We then derived the mean value of the flux at each phase bin, as well as the uncertainty of the mean properly estimated from error propagation. The final average light curve is presented in Figure 1 (a). Typically, the uncertainty of light curve at each phase bin is 300 ppm, which is in consistent with the independent estimate from the bootstrap technique. Here the function `bootstrap` implemented in `scipy` was used. We adopted the default settings except for changing `confidence level = 0.68` to estimate the 1σ error of the mean value.

As mentioned earlier, the Doppler beaming signal is clearly detected in the phase-folded light curve, which should also be carefully considered in the light curve modeling. Under the assumption of radial velocity much smaller than light speed, the beam effect can be expressed as,

$$F_{\lambda} = F_{0,\lambda} \left(1 - B \frac{v}{c}\right), \quad (4)$$

where F_{λ} and $F_{0,\lambda}$ represent the observed flux and emitted flux, respectively. Here v and c are radial velocity and speed of light. B is the beaming factor that is dependent on the wavefront and the relativistic Doppler shift of the target spectrum (with extinction considered) within the TESS photometric band. By using the NLTE synthetic spectrum with the exact parameters from our spectral template matching, we compute synthetic photometric flux at different radial velocities and find the beaming factor B to be 1.2034 for Lan 11.

Light curve fitting with ellc Since the companion should be a compact object, the surface brightness ratio is set to 0 and $R = 0.01R_{\odot}$, providing the companion is a WD. During the light curve modeling, the limb and gravity darkening (with coefficients interpolated from the tables provided by ref.⁵⁷) and the Doppler beaming effects ($B = 1.2034$) were properly considered. The reflection was ignored. In the model, period was fixed to the solution from `LombScargle`, and $T_{\text{eff}}^{\text{sd}}$, $\log g_{\text{sd}}$, R_{sd} and K_{sd} were assumed to be Gaussian distributions with solutions and standard deviations from the spectrum template matching, the SED fitting, and the radial velocity curve fitting. An upper limit $e = 0.02$ yielded by radial velocity curve fitting was also considered. The full settings are summarized in Supplemen-

tary Table 2. Finally, the model includes four free parameters: the orbital inclination i and the superior conjunction time T_0 , $\sqrt{e} \cos \omega$ and $\sqrt{e} \sin \omega$. With above parameter setups in `ellc`, an MCMC approach was performed to sample the light curve by using `EMCEE`⁵⁸. Note that two groups of parameters are yielded by the fitting since the priors of atmospheric parameters ($T_{\text{eff}}^{\text{sd}}$ and $\log g_{\text{sd}}$) can be taken either from the best SNR spectrum or from four phase-picked spectra. As an example, the posterior probability distributions of the parameters with priors from the highest SNR spectrum are shown in Supplementary Figure 9.

Light curve fitting with PHOEBE With the similar parameter setups, the light curve was modeled independently by `PHOEBE`²⁴, which is an open-source python-based module to compute theoretical light and radial velocity curves. We note the gravity darkening is calculated by `PHOEBE` itself with the bolometric gravity brightening coefficient fixed to 1. The coefficients of limb-darkening is interpolated by a logarithmic relation in `PHOEBE` rather than the four-term relation adopted in `ellc`. Again, the posterior probability distributions of the parameters with priors from highest SNR spectrum are shown in Supplementary Figure 10 for an example.

For both `ellc` and `PHOEBE`, we ran 27,000 steps in MCMC. The first 2,000 steps were ignored as burn in. The best-fit results are summarized in Supplementary Table 3. The final adopted values of the orbital and physical parameters of this system were set to an interval ranging from the minimum values minus its 1σ errors to the maximum values plus its 1σ errors from the four groups of estimates determined by the two softwares. The results are listed in Table 1. The model light curves reconstructed by using the best-fit parameters (with priors from the highest SNR spectrum) from `ellc` and `PHOEBE` are shown in Figure 1(a).

The possible nature of the companion star by Binary population synthesis The companion of Lan 11 is strongly suggested to be a compact star by the well-fitted SED from a single hot subdwarf and the non-detection of double-line signal in all of the collected spectra. Here we further explore the nature of this compact object: a CO WD, an ONe WD, or even a NS? Doing so, we performed Monte Carlo binary population synthesis (BPS) calculations to generate WD/NS+hot subdwarf binary populations⁶, by employing the Hurley rapid binary evolution code^{59,60}. The basic assumptions and initial parameters for the Monte Carlo BPS calculations are: (1) All stars are assumed to be members of binaries with circular orbits. (2) The initial mass function of primary stars in the primordial binaries is assumed to follow that from ref.⁶¹, and the mass ratio to follow uniform distribution. (3) The initial distribution of orbital separation a is taken from ref.⁶² that contains a constant value in $\log a$ for the wide binaries (orbital period larger than 100 yr) and a smoothly falling off distribution for close binaries (orbital period smaller than 100 yr). This distribution ensures a roughly equal number of binaries in both wide and close orbits. (4) The common envelope (CE) ejection process plays a very important role in the formation of WD/NS+hot subdwarf binary systems. We adopted the standard energy prescription to deal with the CE ejection process⁶³ by using two free parameters, i.e. the CE ejection parameter α_{CE} and the stellar structure parameter λ . The setting of λ is same as refs.^{64,65}. For the value of α_{CE} , we tried

three groups of values, i.e. 0.5, 0.75, and 1.0, which cover the full range of common adopted values. For each choice of α_{CE} , 2×10^8 primordial binaries are generated and evolved from their births to the formation of WD/NS+hot subdwarf binary systems within Hubble time.

In each of our simulations, LAN 11-like systems are identified by requiring their masses and orbital periods similar to these of Lan 11, i.e., $0.52 \leq M_{\text{sd}} \leq 0.65 M_{\odot}$, $1.08 \leq M_{\text{comp}} \leq 1.35 M_{\odot}$, $|P_{\text{BPS}} - P_{\text{Lan11}}| \leq 200$ min (see Table 1). The nature of the compact star in our BPS simulation is decided by its degenerate CO core mass of its progenitor at the AGB or He giant stage. It is classified as a CO WD if the core mass smaller than $1.088 M_{\odot}$, or as an ONe WD if the core mass ranging from $1.088 M_{\odot}$ to the Chandrasekhar mass limit, or as a NS if the core mass greater than the Chandrasekhar mass limit but less than $6.5 M_{\odot}$ (refs.^{34,25}). The possibilities of LAN 11 like systems with a CO WD, an ONe WD or a NS are then calculated and listed in Supplementary Table 4. In all cases, the probability of ONe WD found in Lan 11-like systems is at least 85%, and the total probability for CO WD and NS is no more than 15%. In this regard, the nature of the compact companion of Lan 11 is most likely an ONe WD.

Evolution of the system The formation and evolutionary models of LAN 11 were investigated via the Modules for Experiments in Stellar Astrophysics (MESA; release 12115)⁶⁶. We applied the ‘‘Dutch’’ wind prescription³¹ with efficiency $\eta = 0.5$ for the wind mass-loss. The metallicity is set to be solar value ($Z = 0.02$). The parameters of mixing length, semi-convective, overshooting are the same as in ref.⁶⁷. In the standard formation channel of hot subdwarf stars⁶⁸, the short orbital period of Lan 11 suggests that its progenitor binary has undergone two phases of common envelope ejection processes. During the CE phase, the star is unable to accrete much of material due to the extremely short timescale⁶³. After the first CE, there is enough time for the He star to expand to fill its Roche lobe before the start of second CE. The companion will accrete mass from this expanding He star, which is the so-called Case BB mass transfer^{33,34}. The mass of the the formed WD is mainly decided by the mass of the He star (see Figure 2 of ref.³⁴).

We then tried to find the progenitor of sdOB star in Lan 11 with a grid of hot subdwarf models. The models are constructed in a way similar to that of ref.⁶⁹, but with masses of progenitors in the range of $2.5 - 3.5 M_{\odot}$. First, the binary enters CE phase when the second one evolved to near the tip of RGB. The envelope was then removed with a high mass-loss rate ($\sim 10^{-3} M_{\odot} \text{ yr}^{-1}$). For each progenitor, the remnant mass is fixed in four cases, i.e. 0.51, 0.55, 0.59, and $0.64 M_{\odot}$, which covers the possible observable interval of Lan 11. Then the hydrogen envelope mass and helium core mass are changed accordingly. By comparisons between the evolutionary tracks and observations (see Supplementary Figure 11), the possible progenitor masses for the hot subdwarf of 0.51, 0.55, 0.59, and $0.64 M_{\odot}$ are 2.6, 2.8, 3.0, and $3.2 M_{\odot}$, respectively. For each sdOB star, if a low-mass progenitor ($\lesssim 2.6 M_{\odot}$) is adopted, the helium core at the RGB is so small that we cannot construct the hot subdwarf models with the corresponding mass. On the other hand, if the progenitor is more massive ($\gtrsim 3.2 M_{\odot}$), none of the evolutionary tracks can match the observations in the $\log T_{\text{eff}}$ -

$\log g$ diagram. The main reason is that the hot subdwarf produced from a massive progenitor generally has a dense envelope due to the hydrogen burning in the shell, which leads to a large value of $\log g$ (small radius) compared to the observations (see also ref.⁷⁰).

The four best-fit models with sdOB mass of 0.51, 0.55, 0.59, and $0.64 M_{\odot}$ are shown in Supplementary Figure 11(a). The tracks start from He core burning with corresponding hydrogen envelope mass of 0.026, 0.030, 0.033, and $0.037 M_{\odot}$, respectively. The relatively large envelope masses are required since the small value of $\log g$ (corresponds to a large radius) of sdOB in Lan 11, as compared to the majority in observations typically resulted from standard thin and light envelope (grey dots in Supplementary Figure 11(a)). For the case of $M_{\text{sd}} \geq 0.55 M_{\odot}$, the sdOB star will fill its Roche lobe due to the shell burning, which leads to the mass transferring to the compact object (see below for detailed explanations). On the contrary, the mass transfer phase will not be initiated for the case of $M_{\text{sd}} < 0.55 M_{\odot}$, where the sdOB radius is always within its Roche lobe.

Finally, we present a representative example of the evolutionary details with $M_{\text{sd}} = 0.59 M_{\odot}$ (corresponding to progenitor mass of $2.8 M_{\odot}$) and compact object mass of $1.29 M_{\odot}$ in Supplementary Figure 11(b). The track starts from He core burning with envelope mass of $0.034 M_{\odot}$, and terminates at the merger event. The He core burning sustains for $\sim 7 \times 10^7$ yr (from stage 1 to 2 as shown in the inset of Supplementary Figure 11(b)). Then the residual hydrogen burning in the envelope leads to the expansion of sdOB radius (from stage 2 to 3), where the current Lan 11 locates between stage 2 and 3. In the subsequent evolutions, we found that the hot subdwarf will undergo two mass transfer phases after He core burning. One is supported by the H burning in the shell (from stage 3 to 4), and another is supported by the He burning in the shell (from stage 6 to 7). After 500-540 Myr, the binary will merge and may end up as an AIC^{1,2}, although the possibility of SNe Ia cannot be fully ruled out⁷. The whole evolution path of this system is summarized in Fig 3(b).

Data Availability

The data supporting the plots in this paper and other findings of this study are available from the corresponding authors upon reasonable request.

Code Availability

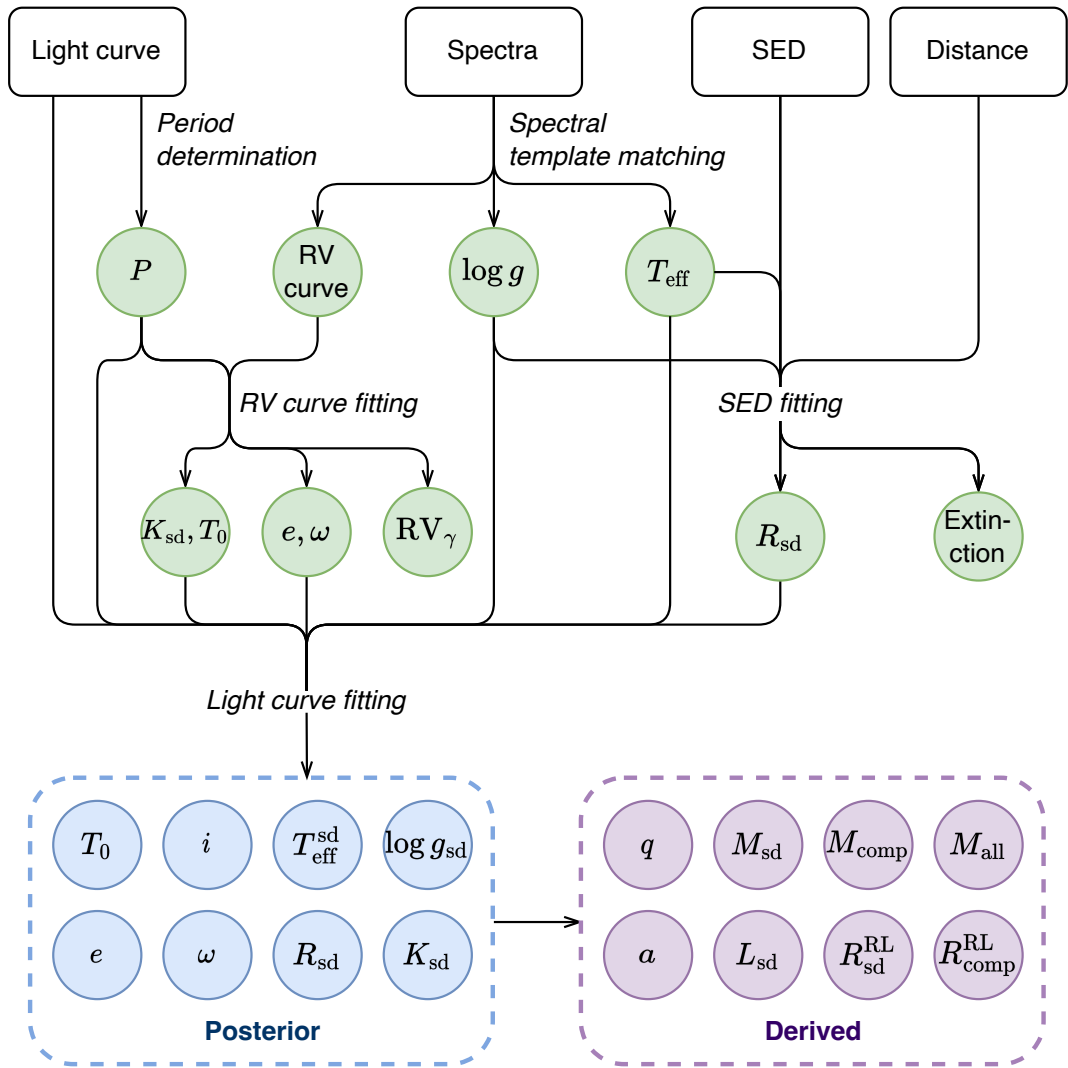
We use standard data analysis tools in the Python environments. Specifically, the Galactic orbital analysis is carried out with Python package `Gala`⁵². TESS light curve is extracted and downloaded with `lightkurve`⁵⁶. Light curve modelling is performed with packages: `phoebe` 2.4.7 and `ellic`²³. MCMC is performed with package `emcee`⁵⁸ 3.1.3. The binary orbital radial velocity is calculated by `radvel`⁴⁷. `mpfit` is available at <https://www.13harrisgeospatial.com/docs/mpfit.html>. The Python packages `astropy`^{43,72}, `numpy`^{73,74} and `scipy`^{75,76} are also used. The DBSP spectra are extracted by `pyexspec`, their radial velocity is measured using package `Laspec`⁴⁶. The SED fitting is performed by using `SPEEDYFIT`. All

Supplementary Table 1: LAMOST Observation Log for Lan 11. For the sake of simplicity, the phase is calculated by fixing $T_0 = 2459477.82316$ derived from radial velocity curve fitting.

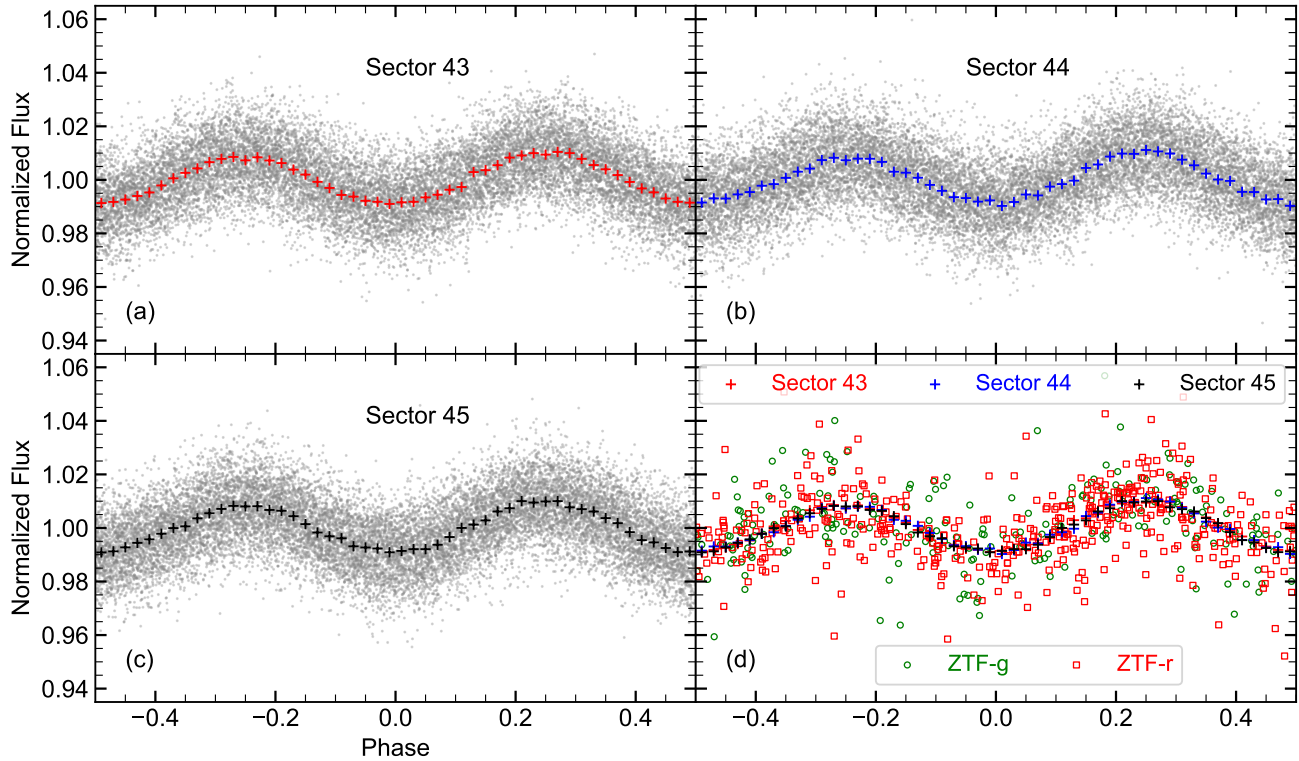
Facility	UT shut yyyy-mm-dd hh:mm:ss	BJDmid day	Exposure s	RV kms ⁻¹	Phase n.a.	SNR n.a.
	2017-10-29T20:18:00	2458056.353515	600	-242.61 ± 6.48	0.139	16.61
	2017-10-29T20:31:00	2458056.362543	600	-243.15 ± 8.05	0.198	14.22
	2017-10-29T20:45:00	2458056.372266	600	-276.79 ± 9.53	0.262	14.20
	2017-10-29T20:58:00	2458056.381295	600	-204.23 ± 7.56	0.321	12.75
	2017-10-29T21:15:00	2458056.393101	600	-144.62 ± 9.59	0.399	14.23
	2017-10-30T20:23:00	2458057.357066	600	233.72 ± 6.52	0.735	16.97
	2017-10-30T20:37:00	2458057.366789	600	201.54 ± 8.47	0.799	14.96
	2017-10-30T20:50:00	2458057.375818	600	161.74 ± 7.16	0.858	18.00
	2017-10-30T21:04:00	2458057.385541	600	97.08 ± 6.43	0.922	17.63
	2017-11-02T19:57:00	2458060.339239	600	-216.32 ± 11.00	0.335	13.78
	2017-11-02T20:16:00	2458060.352435	600	-101.51 ± 11.33	0.422	12.16
	2017-11-02T20:30:00	2458060.362158	600	16.25 ± 11.64	0.486	12.89
	2017-11-04T18:18:00	2458062.270632	600	-100.77 ± 14.43	0.030	6.18
	2017-11-04T18:32:00	2458062.280355	600	-197.21 ± 18.24	0.094	6.68
	2017-11-04T18:45:00	2458062.289384	600	-233.37 ± 12.19	0.153	6.70
	2019-02-21T11:15:00	2458535.979192	1200	81.84 ± 17.51	0.563	8.55
LAMOST	2019-02-21T11:39:00	2458535.995858	1200	229.07 ± 17.51	0.673	10.95
	2019-02-21T12:02:00	2458536.011828	1200	258.95 ± 24.49	0.778	6.80
	2019-02-21T12:26:00	2458536.028494	1200	160.72 ± 15.63	0.888	10.29
	2019-02-21T12:49:00	2458536.044464	1200	24.50 ± 19.07	0.992	6.53
	2019-02-21T13:12:00	2458536.060435	1200	-189.92 ± 20.18	0.097	6.70
	2019-12-05T17:06:00	2458823.225701	1200	155.05 ± 16.86	0.542	11.92
	2019-12-05T17:35:00	2458823.245840	1200	227.73 ± 10.27	0.674	13.28
	2019-12-05T17:58:00	2458823.261813	1200	268.37 ± 18.21	0.779	12.27
	2021-01-20T12:41:00	2459235.041135	1200	-296.58 ± 17.39	0.272	11.01
	2021-01-20T13:04:00	2459235.057106	1200	-162.81 ± 14.80	0.377	9.32
	2021-01-20T13:28:00	2459235.073772	1200	-15.29 ± 16.11	0.487	9.15
	2021-01-30T12:40:00	2459245.039865	1200	-39.25 ± 23.59	0.991	8.38
	2021-01-30T13:04:00	2459245.056530	1200	-187.26 ± 10.68	0.100	9.80
	2021-01-30T13:27:00	2459245.072501	1200	-247.41 ± 10.71	0.205	11.63
	2021-02-02T13:57:00	2459248.093134	1200	-107.73 ± 8.20	0.059	14.11
	2021-02-02T14:21:00	2459248.109799	1200	-241.51 ± 10.39	0.168	13.23
	2021-02-02T14:47:00	2459248.127854	1200	-214.24 ± 9.60	0.287	13.02
	2021-02-20T11:15:00	2459265.979227	1200	185.05 ± 19.69	0.618	8.13

Supplementary Table 2: DBSP Observation Log for Lan 11. For the sake of simplicity, the phase is calculated by fixing $T_0 = 2459477.82316$ derived from fitting radial velocity curve. The four spectra marked with * are selected for spectral fits.

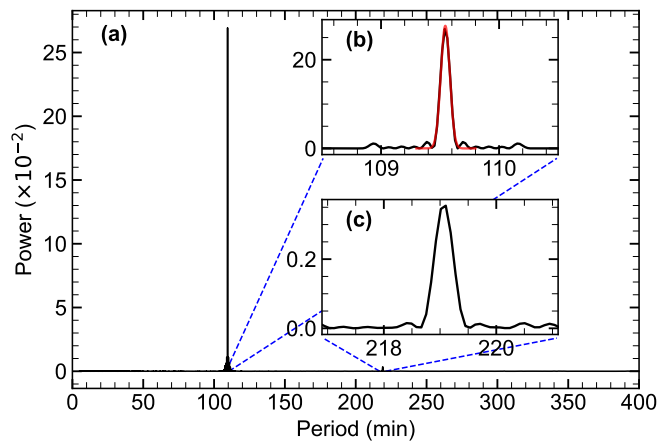
Facility	UT shut yyyy-mm-dd hh:mm:ss	BJDmid day	Exposure s	RV kms^{-1}	Phase n.a.	SNR n.a.
	2022-02-19T03:35:50*	2459629.657012	600	78.29 ± 0.97	0.955	137.79
	2022-02-19T03:59:21*	2459629.673343	600	-98.39 ± 1.39	0.062	110.51
	2022-02-19T04:14:19	2459629.683740	600	-208.10 ± 0.78	0.131	105.52
	2022-02-19T04:24:41	2459629.690935	600	-244.49 ± 0.91	0.178	102.13
	2022-02-19T04:35:02	2459629.698130	600	-261.65 ± 1.32	0.225	100.98
	2022-02-19T04:45:24	2459629.705325	600	-255.03 ± 1.05	0.272	100.91
	2022-02-19T04:55:46*	2459629.712520	600	-230.00 ± 0.84	0.320	108.16
	2022-02-19T05:06:08	2459629.719714	600	-183.23 ± 1.07	0.367	103.04
	2022-02-19T05:16:29	2459629.726909	600	-121.69 ± 1.26	0.414	105.22
	2022-02-19T05:26:51*	2459629.734104	600	-50.00 ± 1.06	0.462	110.40
	2022-02-19T05:37:13	2459629.741299	600	20.23 ± 0.78	0.509	107.77
	2022-02-19T05:47:34	2459629.748493	600	98.65 ± 1.42	0.556	104.29
	2022-02-19T05:57:56	2459629.755688	600	155.28 ± 1.20	0.603	93.76
P200 DBSP	2022-02-19T06:19:17	2459629.770510	600	236.04 ± 1.29	0.701	83.41
	2022-02-19T06:29:38	2459629.777704	600	241.38 ± 1.04	0.748	94.08
	2022-02-19T06:40:00	2459629.784899	600	221.57 ± 1.52	0.795	93.00
	2022-02-19T06:50:22	2459629.792094	600	187.36 ± 1.10	0.843	94.79
	2022-02-19T07:00:43	2459629.799289	600	138.03 ± 1.80	0.890	92.90
	2022-02-19T07:11:05	2459629.806484	600	85.85 ± 0.91	0.937	96.11
	2022-02-19T07:21:27	2459629.813679	600	11.39 ± 1.02	0.985	94.41
	2022-02-19T07:31:48	2459629.820873	600	-62.87 ± 1.39	0.032	92.46
	2022-02-19T07:42:10	2459629.828068	600	-133.19 ± 1.06	0.079	90.19
	2022-02-19T08:02:06	2459629.841904	600	-230.00 ± 1.04	0.170	84.26
	2022-02-19T08:12:27	2459629.849099	600	-253.75 ± 1.49	0.217	85.53
	2022-02-19T08:22:49	2459629.856294	600	-255.63 ± 1.45	0.265	82.68
	2022-02-19T08:33:11	2459629.863489	600	-223.88 ± 1.49	0.312	73.21
	2022-02-19T08:43:32	2459629.870684	600	-180.00 ± 1.28	0.359	70.06
	2022-02-19T08:53:54	2459629.877878	600	-124.83 ± 1.98	0.407	68.19



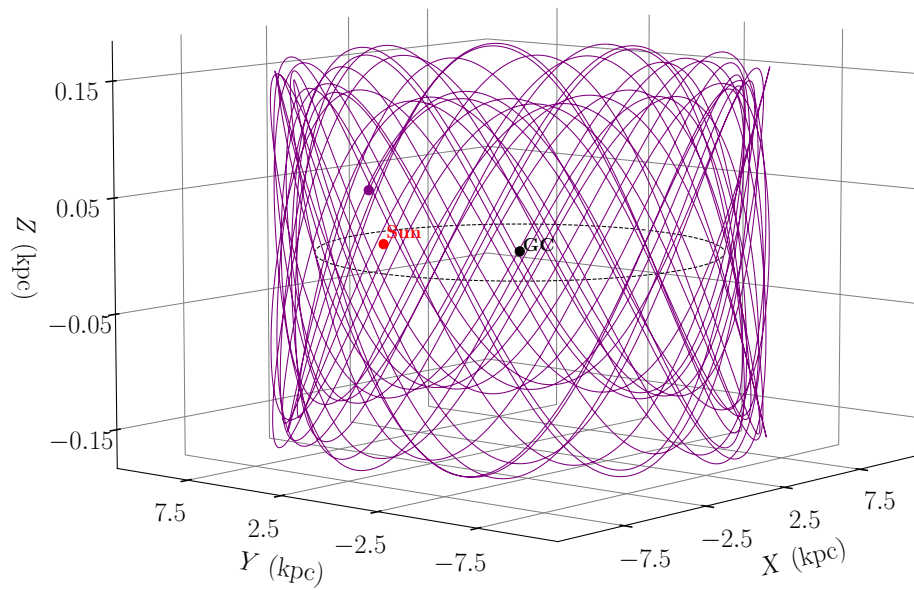
Supplementary Figure 1 – Flowchart of estimates of stellar properties and orbital parameters for Lan 11.



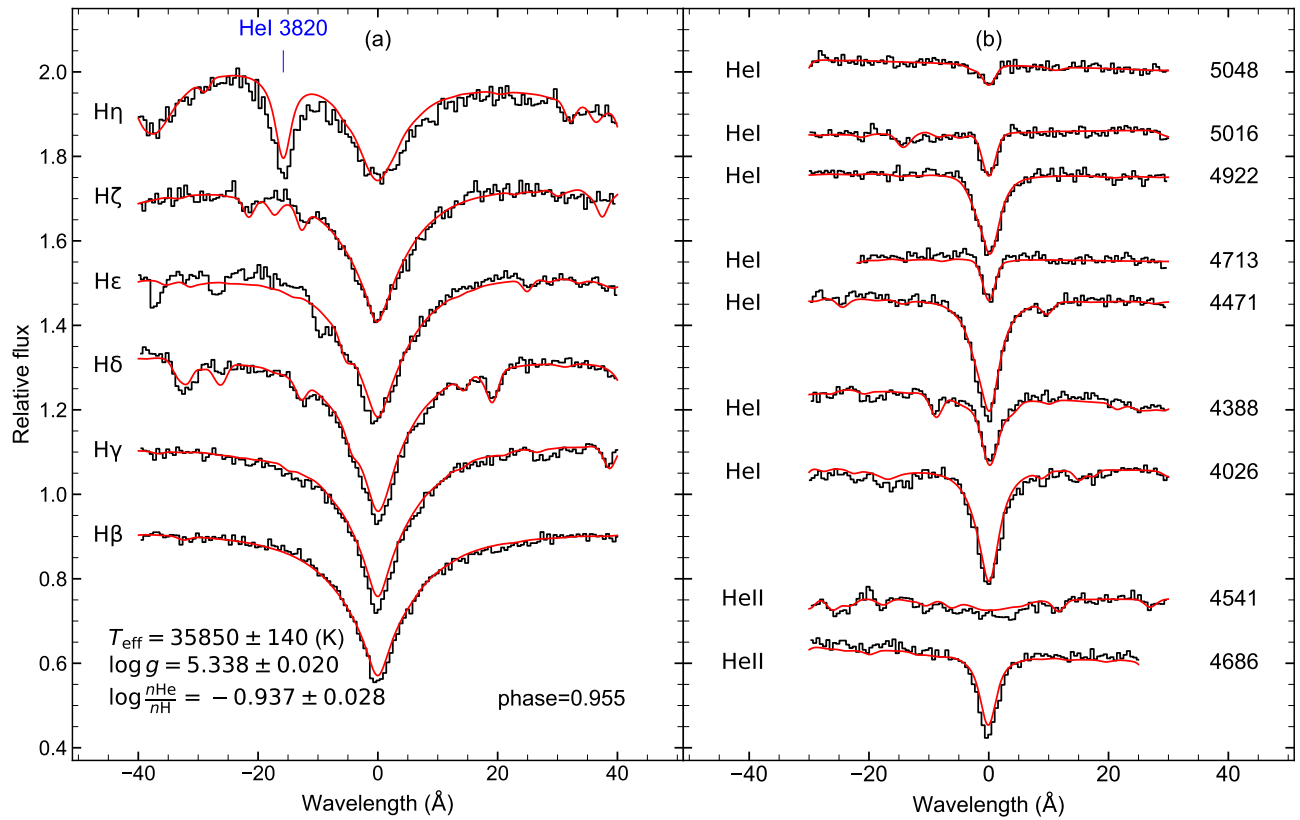
Supplementary Figure 2 – Phase folded TESS and ZTF light curves. Panels (a)-(c) show the phase folded light curves for TESS Sector 43, 44 and 45, respectively. The cross symbols represent the median values of the TESS fluxes within bins from phase -0.5 to 0.5 at a step 0.02 . Panel (d) shows the light curves for ZTF g (green circle) and r (red square), respectively. The median TESS light curves are also overplotted for comparisons.



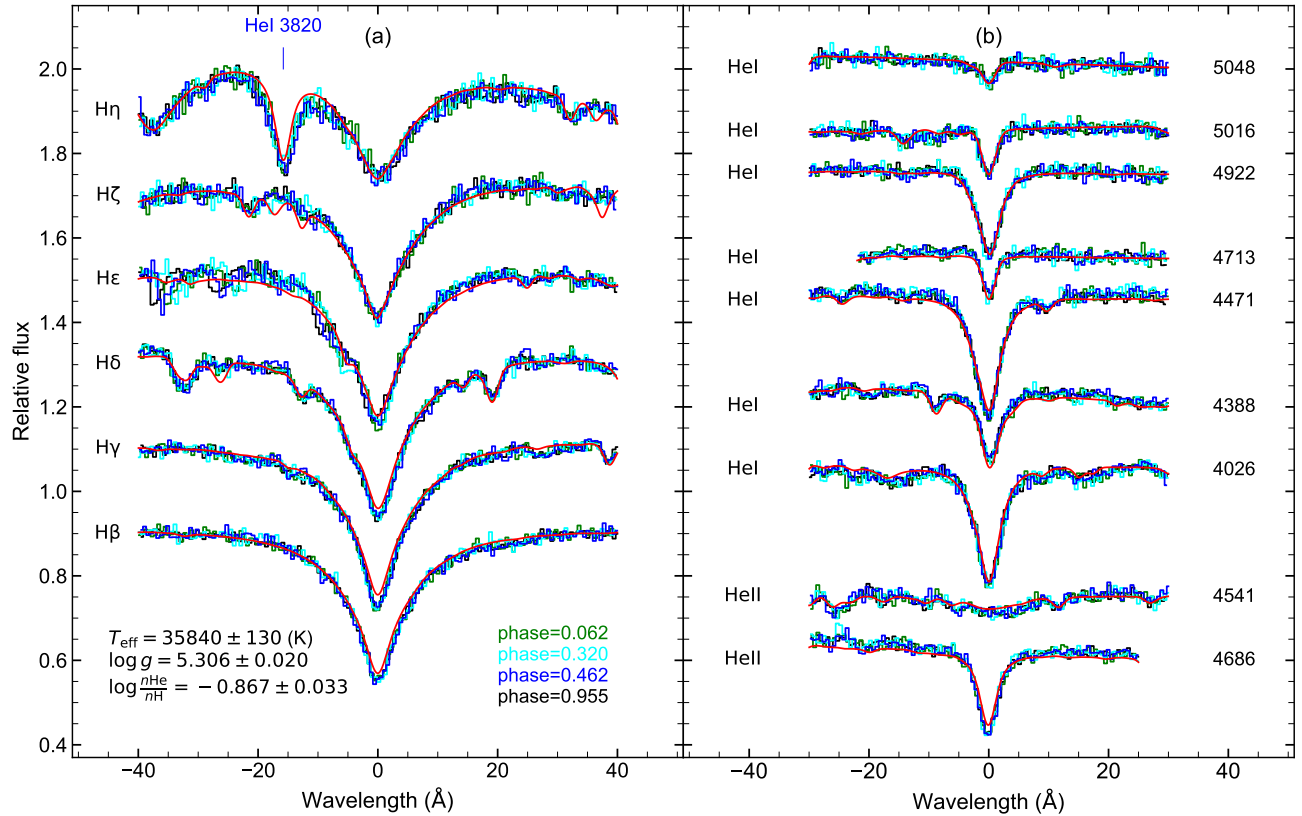
Supplementary Figure 3 – The Lomb–Scargle periodogram of the TESS light curve. In the full periodogram, a dominant peak can be seen at $109.54440(20)$ min, corresponding to half of the orbital period. *Panel (b)*: the red line is the best-fit Gaussian function using non-linear least squares to fit the periodogram data around the peak period. The error is the square root of the estimated covariance. *Panel (c)*: the peak of the second harmonic arising from the Doppler beaming effect.



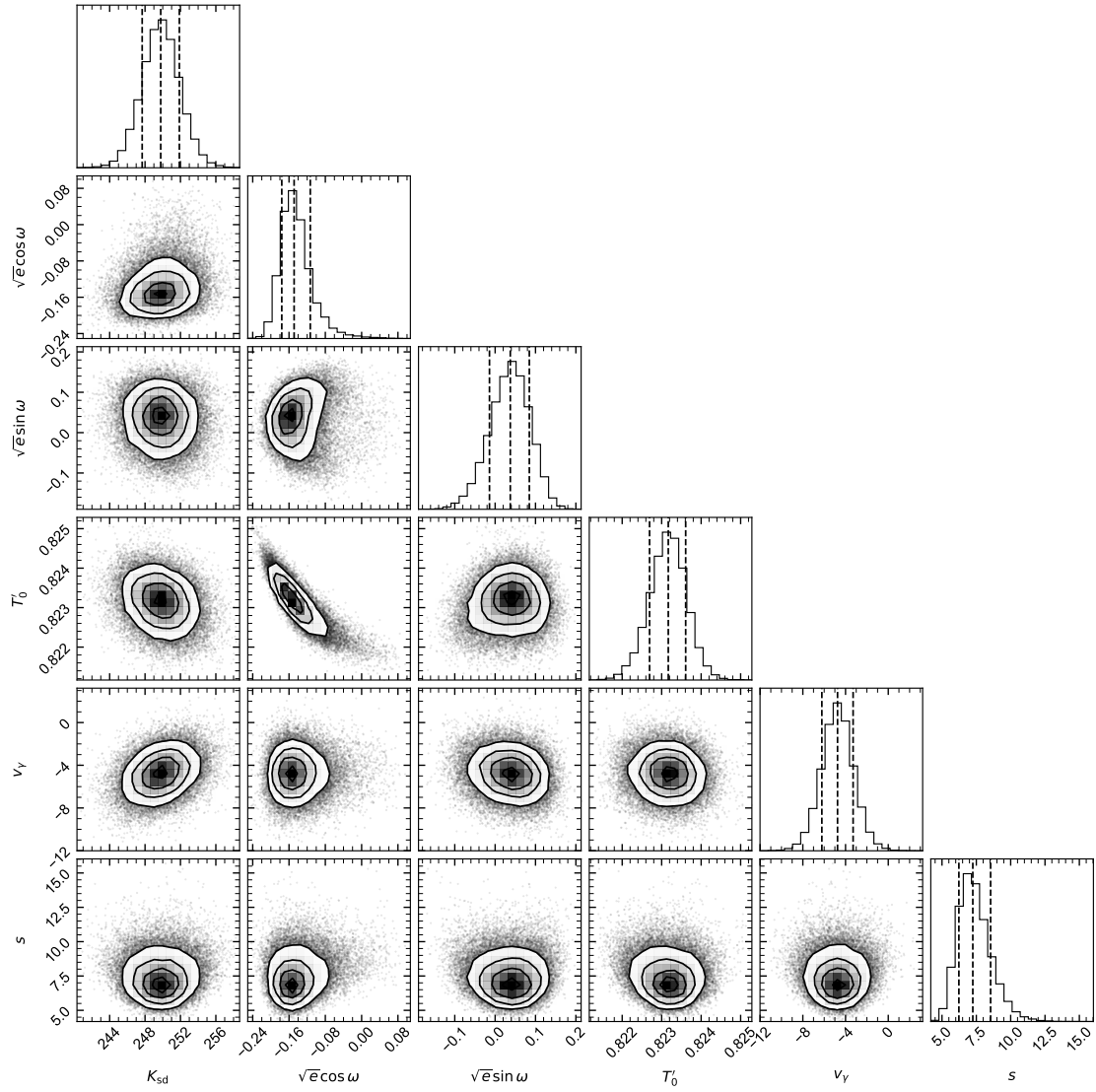
Supplementary Figure 4 – 3D representation of the backward orbit of Lan 11. The orbit is integrated up to 5 Gyr back in time with a step of 0.1 Myr. The purple dot marks the current positions of Lan 11. The red and black dots represent the positions of the Sun and the Galactic Center, respectively. The Solar circle ($R = 8.178$ kpc) is marked by the dotted gray lines.



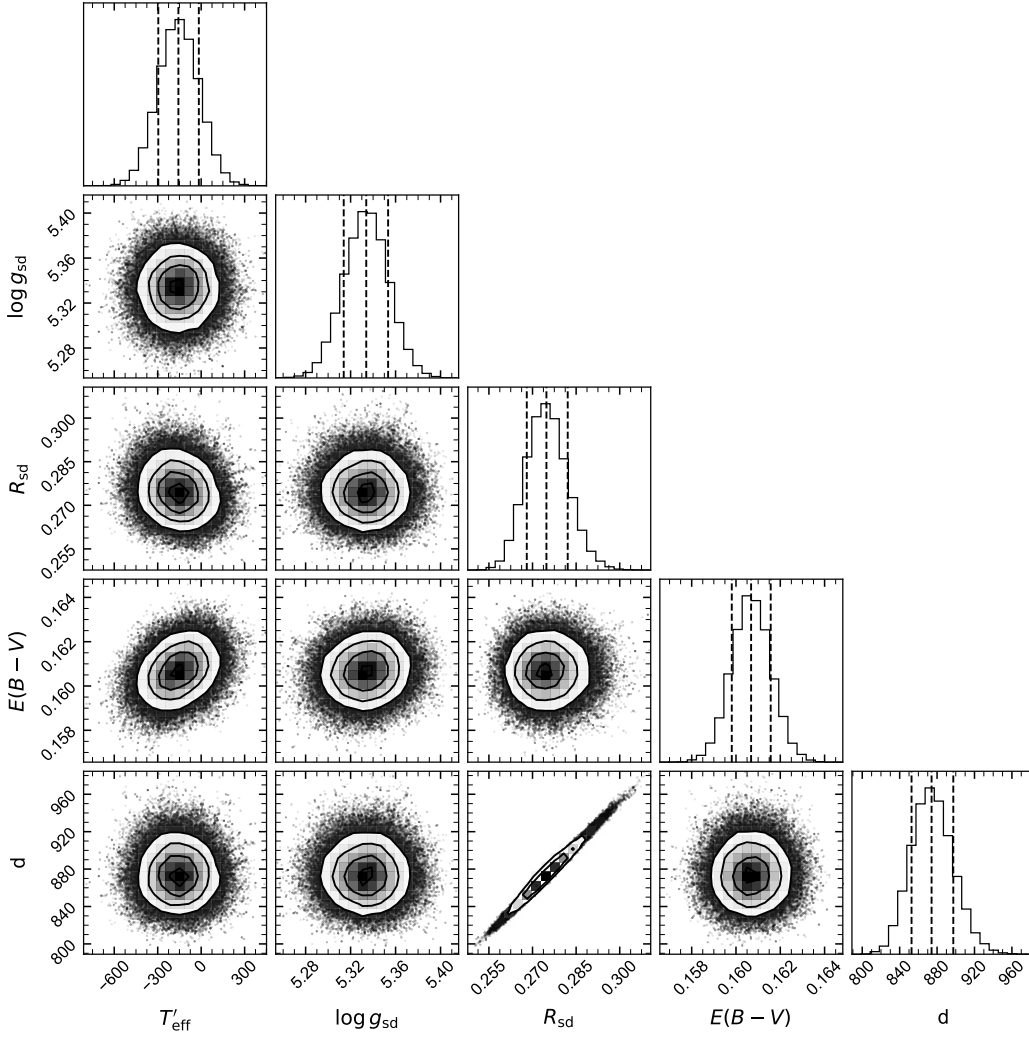
Supplementary Figure 5 – Spectral fit to highest SNR DBSP spectrum. Panels (a) and (b) show the fit to the hydrogen and helium lines of the highest SNR DBSP spectrum observed at the orbital phase of 0.955. The observed spectral lines are shown in black, and the best-fit model lines are shown in red. The best-fit parameters are shown in the bottom-left corner of panel (a).



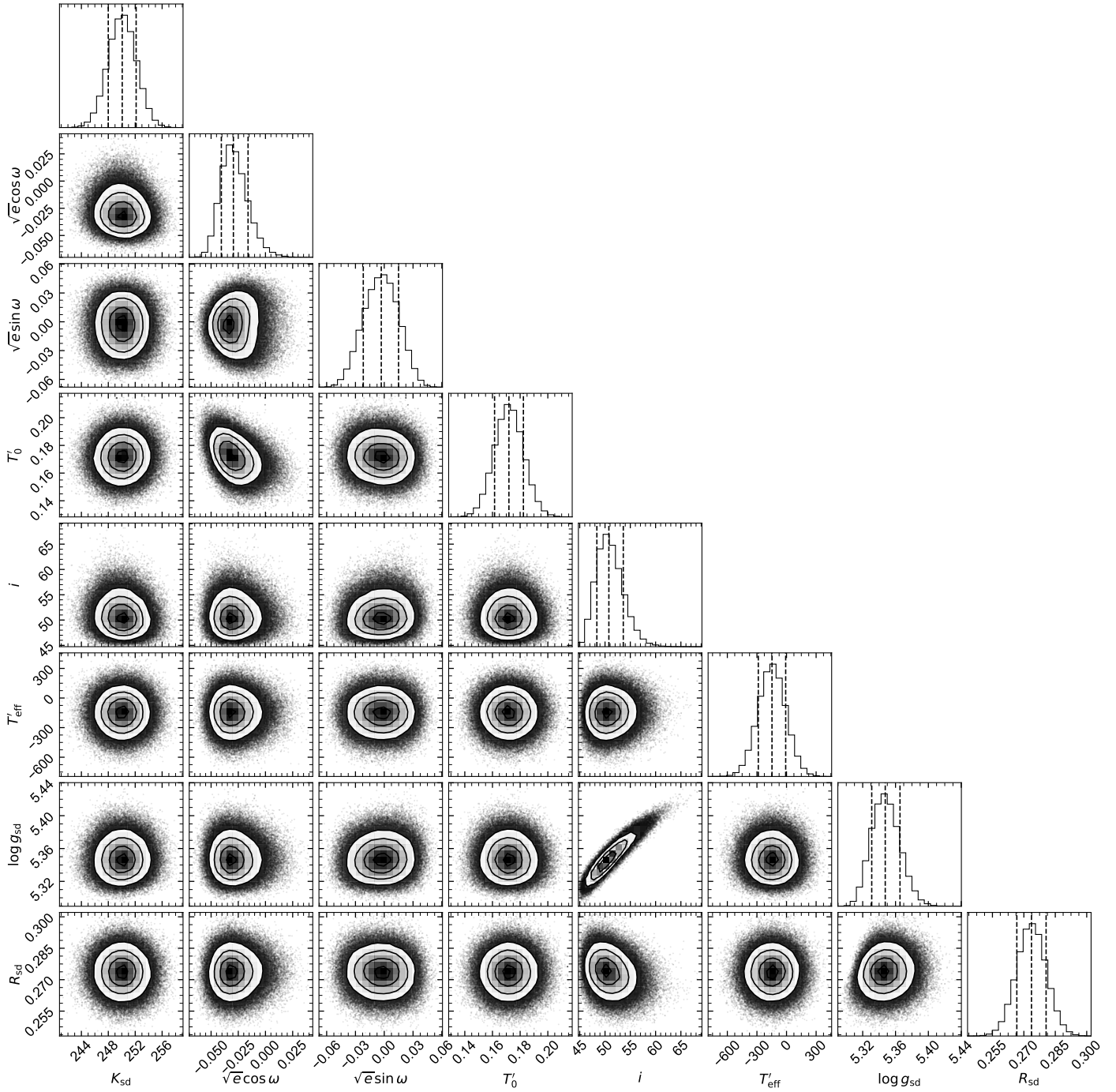
Supplementary Figure 6 – Spectral fit to four phase-picked DBSP spectra. Panels (a) and (b) show the fit to the hydrogen and helium lines of four phase-picked high-SNR spectra. The orbital phase of each spectrum is marked in the bottom-right corner of panel (a). The observed spectral lines are shown in green, cyan, blue, and black, and the best-fit model lines are shown in red. The best-fit parameters are shown in the bottom-left corner of panel (a).



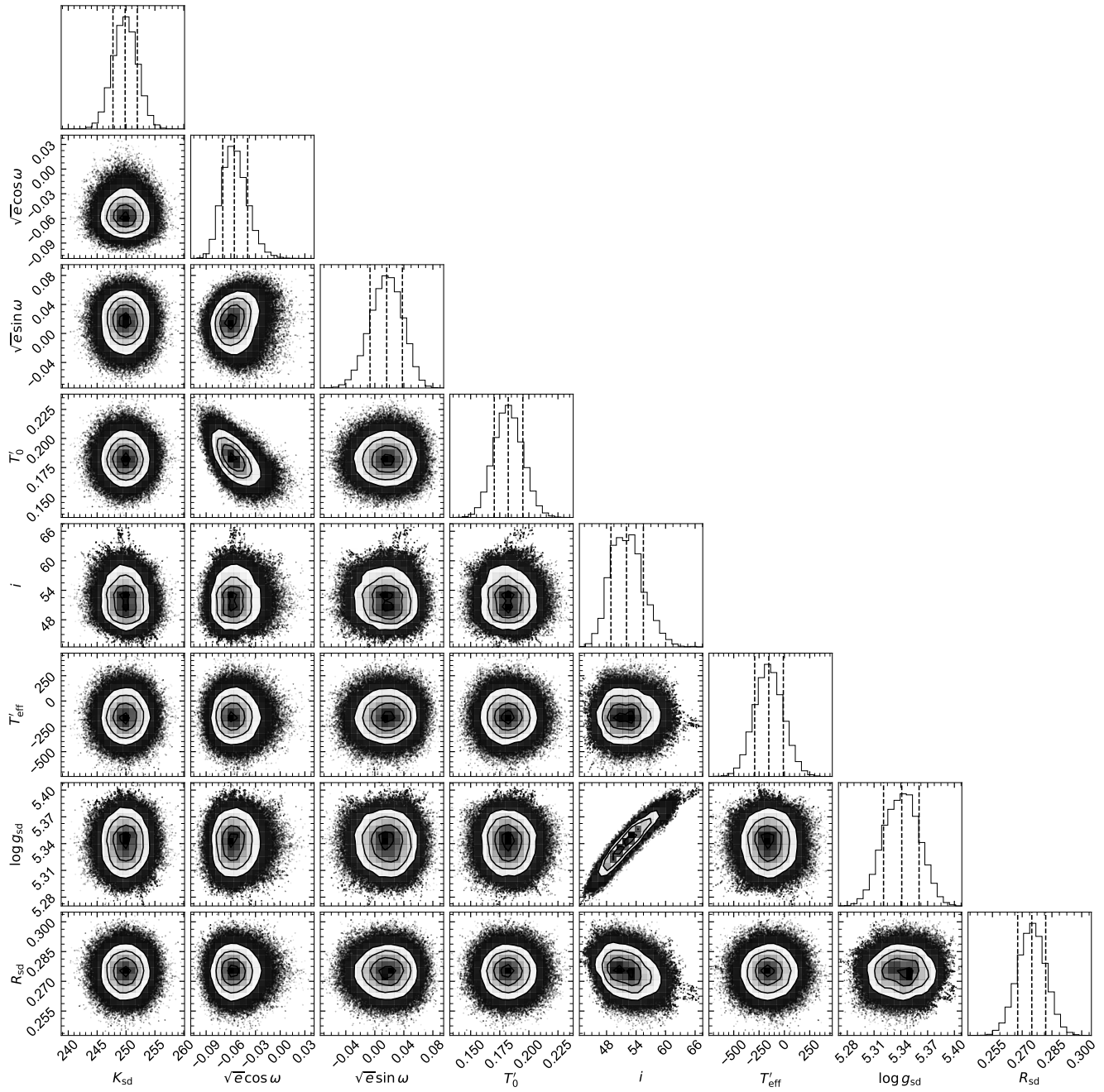
Supplementary Figure 7 – Corner plot for the MCMC sampling of the radial velocity curve. Posterior probability distribution of the parameters directly derived by the MCMC simulation based on the radial velocity curve measured from the DBSP spectra. Note that $T_0' = T_0 - 2459477$ is in BJD, K_{sd} , v_γ and s are in km s^{-1} , and s is the jitter.



Supplementary Figure 8 – Corner plot for the SED MCMC sampling using `speedyfit`. Posterior probability distribution of the parameters directly derived by the MCMC simulation based on the multi-band photometry, including *Gaia* EDR3 G_{bp} -, G - and G_{rp} -bands, PanSTARRS z - and y -bands, 2MASS J -, H - and K_s -bands, and ALLWISE W_1 -, W_2 -bands. The effective temperature of hot subdwarf $T_{\text{eff}} = T'_{\text{eff}} + 36000$ K. R_{sd} is the radius of the hot subdwarf in solar radius; $\log g_{\text{sd}}$ is the surface gravity of hot subdwarf star, $E(B - V)$ is extinction in magnitude, and d is the distance in parsec.



Supplementary Figure 9 – Corner plot for the MCMC sampling of the light curve using e11c. Posterior probability distribution of the parameters directly derived by the MCMC simulation based on the TESS light curve. Labels shown are the semi-amplitude radial velocity of the hot subdwarf K_{sd} in km s^{-1} , the longitude of periastron ω in degree, eccentricity e , the superior conjunction time T_0 in BJD, $T'_0 = (T_0 - 2459477.82) \times 100$, binary orbital inclination angle i in degree, the effective surface temperature of the hot subdwarf $T'_{\text{eff}} = T_{\text{eff}} + 36000 \text{ K}$, the surface gravity $\log g_{sd}$, and the radius of hot subdwarf R_{sd} in solar radius.



Supplementary Figure 10 – Corner plot for the MCMC sampling of the light curve using PHOEBE. Posterior probability distribution of the parameters directly derived by the MCMC simulation based on the TESS light curve using PHOEBE. The labels are same as these in Supplementary Figure 9.

Supplementary Table 3: Results from light curve fitting based on different software packages and priors. \mathcal{N} and \mathcal{U} represent normal and uniform distributions, respectively. Quoted values are the median, and uncertainties denote the 68% confidence interval.

Prior		219.08880 (fixed)			
Prior	P (min)	$\mathcal{N}(249.8, 2.1)$			
	K_{sd}	$\mathcal{U}(-0.10, 0.10)$			
	$\sqrt{e} \cos \omega$	$\mathcal{U}(-0.10, 0.10)$			
	$\sqrt{e} \sin \omega$	$\mathcal{U}(0.81, 0.83)$			
	T_0 (BJD-24572477)	$\mathcal{U}(0, 1)$			
	$\cos i$				
	T_{eff}^{sd}	$\mathcal{N}(35840, 130)$	$\mathcal{N}(35850, 140)$		
$\log g_{sd}$	$\mathcal{N}(5.306, 0.02)$	$\mathcal{N}(5.338, 0.02)$			
R_{sd}	$\mathcal{N}(0.275, 0.007)$	$\mathcal{N}(0.275, 0.007)$			
		ellc	PHOEBE	ellc	PHOEBE
Posterior	K_{sd} (km s ⁻¹)	249.9 ^{+2.1} _{-2.1}	249.7 ^{+2.0} _{-2.1}	250.1 ^{+2.1} _{-2.1}	249.7 ^{+2.0} _{-2.1}
	$\sqrt{e} \cos \omega$	-0.029 ^{+0.014} _{-0.011}	-0.056 ^{+0.016} _{-0.014}	-0.029 ^{+0.014} _{-0.011}	-0.056 ^{+0.016} _{-0.014}
	$\sqrt{e} \sin \omega$	-0.004 ^{+0.019} _{-0.019}	0.014 ^{+0.022} _{-0.022}	-0.003 ^{+0.018} _{-0.019}	0.016 ^{+0.022} _{-0.023}
	T_0 (BJD-2459477)	0.82172(11)	0.82182(13)	0.82172(11)	0.82182(13)
	i (°)	48.3 ^{+2.0} _{-1.6}	47.9 ^{+2.5} _{-2.5}	50.8 ^{+2.8} _{-2.4}	52.1 ^{+3.4} _{-3.2}
	T_{eff}^{sd}	35841 ⁺¹³¹ ₋₁₃₁	35839 ⁺¹²⁷ ₋₁₂₅	35853 ⁺¹³⁹ ₋₁₃₉	35845 ⁺¹⁴³ ₋₁₃₉
	$\log g_{sd}$ [cm s ⁻²]	5.328 ^{+0.014} _{-0.012}	5.312 ^{+0.018} _{-0.020}	5.347 ^{+0.018} _{-0.016}	5.341 ^{+0.019} _{-0.020}
R_{sd} (R_{\odot})	0.272 ± 0.007	0.275 ± 0.007	0.274 ± 0.007	0.275 ± 0.007	
Derived	q	2.18 ^{+0.16} _{-0.17}	2.24 ^{+0.24} _{-0.21}	1.98 ^{+0.18} _{-0.18}	1.92 ^{+0.22} _{-0.19}
	M_{sd} (M_{\odot})	0.577 ^{+0.039} _{-0.037}	0.563 ^{+0.039} _{-0.039}	0.609 ^{+0.042} _{-0.040}	0.603 ^{+0.042} _{-0.040}
	M_{comp} (M_{\odot})	1.258 ^{+0.066} _{-0.068}	1.258 ^{+0.095} _{-0.083}	1.203 ^{+0.078} _{-0.077}	1.158 ^{+0.091} _{-0.083}
	M_{all} (M_{\odot})	1.834 ^{+0.083} _{-0.083}	1.823 ^{+0.099} _{-0.092}	1.812 ^{+0.089} _{-0.088}	1.765 ^{+0.095} _{-0.092}
	a (R_{\odot})	1.468 ^{+0.022} _{-0.022}	1.465 ^{+0.026} _{-0.025}	1.462 ^{+0.024} _{-0.024}	1.449 ^{+0.026} _{-0.026}
	L_{sd} (L_{\odot})	110.2 ^{+5.8} _{-5.7}	112.0 ^{+6.1} _{-5.8}	111.5 ^{+6.0} _{-5.9}	112.4 ^{+6.0} _{-6.1}
	$R_{sd}^{Roche-lobe}$ (R_{\odot})	0.461 ^{+0.011} _{-0.011}	0.457 ^{+0.011} _{-0.012}	0.470 ^{+0.012} _{-0.011}	0.470 ^{+0.012} _{-0.012}
$R_{comp}^{Roche-lobe}$ (R_{\odot})	0.658 ^{+0.014} _{-0.015}	0.659 ^{+0.022} _{-0.019}	0.642 ^{+0.018} _{-0.018}	0.632 ^{+0.022} _{-0.020}	

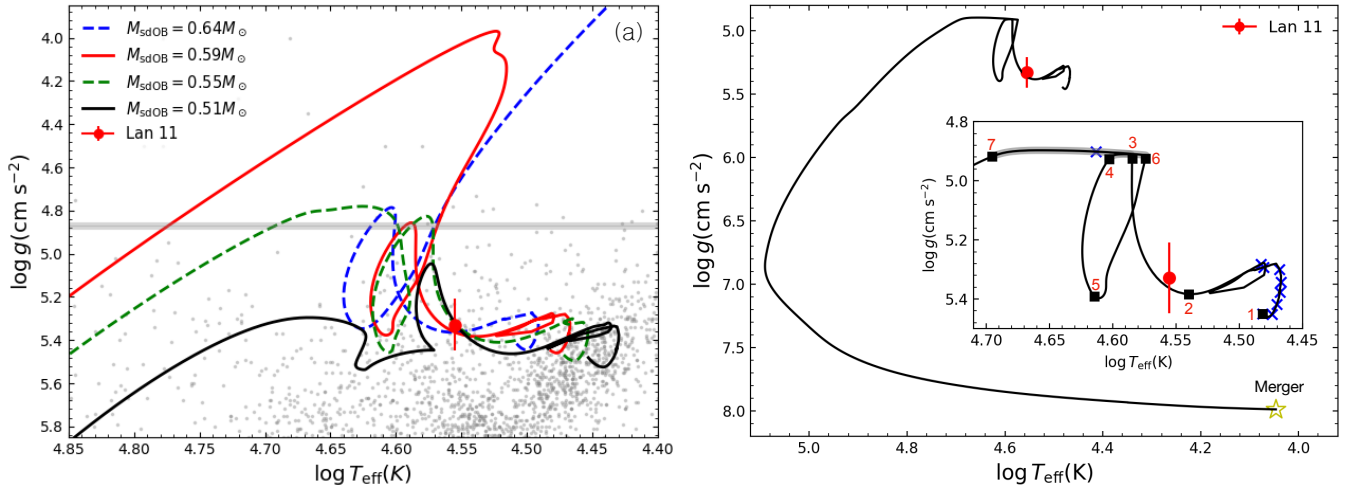
Supplementary Table 4: Natures of compact companion of Lan 11 as revealed by our binary population synthesis simulations.

α_{CE}	CO WD	ONe WD	NS
0.5	7%	90%	3%
0.75	11%	87%	2%
1.0	9%	85%	6%

module mentioned above are publicly available. XTGRID is publicly available online at www.Astroserver.org. The Hurley rapid binary evolution code^{59,60} is publicly available online at <https://astronomy.swin.edu.au/~jhurley/>. The binary evolutionary model is carried out with MESA 12115⁶⁶.

References

- Miyaji, S., Nomoto, K., Yokoi, K. & Sugimoto, D. Supernova triggered by electron captures. *PASJ* **32**, 303–329 (1980).
- Nomoto, K. Evolution of 8-10 solar mass stars toward electron capture supernovae. I - Formation of electron-degenerate O + NE + MG cores. *Astrophys. J.* **277**, 791–805 (1984).
- Tauris, T. M., Sanyal, D., Yoon, S. C. & Langer, N. Evolution towards and beyond accretion-induced collapse of massive white dwarfs and formation of millisecond pulsars. *Astron. Astrophys.* **558**, A39 (2013).
- Liu, W.-M. & Li, X.-D. Evolution of Post-accretion-induced Collapse Binaries: The Effect of Evaporation. *Astrophys. J.* **851**, 58 (2017).
- Wang, B. & Liu, D. The formation of neutron star systems through accretion-induced collapse in white-dwarf binaries. *Research in Astronomy and Astrophysics* **20**, 135 (2020).
- Liu, D. & Wang, B. The formation of single neutron stars from double white-dwarf mergers via accretion-induced collapse. *Mon. Not. R. Astron. Soc.* **494**, 3422–3431 (2020).
- Marquardt, K. S. et al. Type Ia supernovae from exploding oxygen-neon white dwarfs. *Astron. Astrophys.* **580**, A118 (2015).
- Boyles, J. et al. Young Radio Pulsars in Galactic Globular Clusters. *Astrophys. J.* **742**, 51 (2011).
- Bailyn, C. D. & Grindlay, J. E. Neutron Stars and Millisecond Pulsars from Accretion-induced Collapse in Globular Clusters. *Astrophys. J.* **353**, 159 (1990).
- Liu, D., Wang, B., Chen, W., Zuo, Z. & Han, Z. Evolving ONe WD+He star systems to intermediate-mass binary pulsars. *Mon. Not. R. Astron. Soc.* **477**, 384–391 (2018).
- Liu, D. & Wang, B. Evolving ONe WD+He WD systems to ultra-compact X-ray binaries. *Mon. Not. R. Astron. Soc.* **521**, 6053–6060 (2023).
- Margalit, B., Berger, E. & Metzger, B. D. Fast Radio Bursts from Magnetars Born in Binary Neutron Star Mergers and Accretion Induced Collapse. *Astrophys. J.* **886**, 110 (2019).
- Ruijter, A. J. et al. On the formation of neutron stars via accretion-induced collapse in binaries. *Mon. Not. R. Astron. Soc.* **484**, 698–711 (2019).



Supplementary Figure 11 – The evolutionary tracks of a LAN 11-like sdOB-WD binary system. Panel a: Hot subdwarf tracks with different masses: $M_{\text{sdOB}} = 0.51, 0.55, 0.59, 0.64 M_{\odot}$ (with corresponding progenitor masses: 2.6, 2.8, 3.0, 3.2 M_{\odot}). The location of Lan 11 is shown in red dot, and the grey dots represent the observational sample of sdOB stars taken from ref.⁷¹. The grey line represents the approximate position of $\log g$ if the sdOB star radius approaches to the Roche lobe radius. It is noted that the sdOB star with mass of $0.51 M_{\odot}$ would never fills its Roche lobe. Panel b: The evolutionary details of a Lan 11-like system with $M_{\text{sdOB}} = 0.59 M_{\odot}$ and a compact companion of $1.29 M_{\odot}$. The track starts from He core burning, and ends at the merger event, as shown in the yellow star. In the inset, the blue crosses mark the time interval of 10^7 yr. The black squares represent different evolution states: He core burning (1), H burning in the shell (2), the onset of the first mass transfer phase (3), the termination of the first mass transfer phase (4), the He burning in the shell (5), the onset of the second mass transfer phase (6), and the termination of the mass transfer phase (7). The mass transfer phase is shown in a thick black line.

14. Gaia Collaboration et al. Gaia Data Release 3: Summary of the content and survey properties. [arXiv e-prints arXiv:2208.00211](#) (2022).
15. Lindgren, L. et al. Gaia Early Data Release 3. Parallax bias versus magnitude, colour, and position. *Astron. Astrophys.* **649**, A4 (2021).
16. Lei, Z., Zhao, J., Németh, P. & Zhao, G. New Hot Subdwarf Stars Identified in Gaia DR2 with LAMOST DR5 Spectra. *Astrophys. J.* **868**, 70 (2018).
17. Maxted, P. F. L., Marsh, T. R. & North, R. C. KPD 1930+2752: a candidate Type Ia supernova progenitor. *Mon. Not. R. Astron. Soc.* **317**, L41–L44 (2000).
18. Pelisoli, I. et al. A hot subdwarf-white dwarf super-Chandrasekhar candidate supernova Ia progenitor. *Nature Astronomy* **5**, 1052–1061 (2021).
19. Arenas, J., Catalán, M. S., Augusteijn, T. & Retter, A. A spectroscopic study of V603 Aquilae: stellar parameters and continuum-line variations. *Mon. Not. R. Astron. Soc.* **311**, 135–148 (2000).
20. Thoroughgood, T. D., Dhillon, V. S., Littlefair, S. P., Marsh, T. R. & Smith, D. A. The mass of the white dwarf in the recurrent nova U Scorpii. *Mon. Not. R. Astron. Soc.* **327**, 1323–1333 (2001).
21. Németh, P. XTRID Live: Online Spectral Analyses with TLUSTY Models. In Werner, K., Stehle, C., Rauch, T. & Lanz, T. (eds.) *Radiative Signatures from the Cosmos*, vol. 519 of *Astronomical Society of the Pacific Conference Series*, 117 (2019). 1901.04742.
22. Green, G. M., Schlafly, E., Zucker, C., Speagle, J. S. & Finkbeiner, D. A 3D Dust Map Based on Gaia, Pan-STARRS 1, and 2MASS. *Astrophys. J.* **887**, 93 (2019).
23. Maxted, P. F. L. ellc: A fast, flexible light curve model for detached eclipsing binary stars and transiting exoplanets. *Astron. Astrophys.* **591**, A111 (2016).
24. Prša, A. & Zwitter, T. A Computational Guide to Physics of Eclipsing Binaries. I. Demonstrations and Perspectives. *Astrophys. J.* **628**, 426–438 (2005).
25. Lauffer, G. R., Romero, A. D. & Kepler, S. O. New full evolutionary sequences of H- and He-atmosphere massive white dwarf stars using MESA. *Mon. Not. R. Astron. Soc.* **480**, 1547–1562 (2018).
26. Toonen, S., Perets, H. B., Igoshev, A. P., Michaely, E. & Zenati, Y. The demographics of neutron star - white dwarf mergers. Rates, delay-time distributions, and progenitors. *Astron. Astrophys.* **619**, A53 (2018).
27. Geier, S. et al. A progenitor binary and an ejected mass donor remnant of faint type Ia supernovae. *Astron. Astrophys.* **554**, A54 (2013).
28. Santander-García, M. et al. The double-degenerate, super-Chandrasekhar nucleus of the planetary nebula Henize 2-428. *Nature* **519**, 63–65 (2015).
29. Napiwotzki, R. et al. The ESO supernovae type Ia progenitor survey (SPY). The radial velocities of 643 DA white dwarfs. *Astron. Astrophys.* **638**, A131 (2020).
30. Kupfer, T. et al. Discovery of a Double-detonation Thermonuclear Supernova Progenitor. *Astrophys. J.* **925**, L12 (2022).
31. Glebbeek, E., Gaburov, E., de Mink, S. E., Pols, O. R. & Portegies Zwart, S. F. The evolution of runaway stellar collision products. *Astron. Astrophys.* **497**, 255–264 (2009).
32. Ge, H., Webbink, R. F. & Han, Z. The Thermal Equilibrium Mass-loss Model and Its Applications in Binary Evolution. *Astrophys. J. Supp.* **249**, 9 (2020).
33. Savonije, G. J. & Takens, R. J. Evolution of helium stars: a self-consistent determination of the boundary of a helium burning convective core. *Astron. Astrophys.* **47**, 231–241 (1976).
34. Tauris, T. M., Langer, N. & Podsiadlowski, P. Ultra-stripped supernovae: progenitors and fate. *Mon. Not. R. Astron. Soc.* **451**, 2123–2144 (2015).
35. Shen, K. J. & Bildsten, L. The Ignition of Carbon Detonations via Converging Shock Waves in White Dwarfs. *Astrophys. J.* **785**, 61 (2014).
36. Bellm, E. C. et al. The Zwicky Transient Facility: System Overview, Performance, and First Results. *PASP* **131**, 018002 (2019).

37. Jiang, P. *et al.* The fundamental performance of FAST with 19-beam receiver at L band. *Research in Astronomy and Astrophysics* **20**, 064 (2020).
38. Hotan, A. W., van Straten, W. & Manchester, R. N. PSRCHIVE and PSRFITS: An Open Approach to Radio Pulsar Data Storage and Analysis. *Publ. Astron. Soc. Aust.* **21**, 302–309 (2004).
39. Cordes, J. M. & Lazio, T. J. W. NE2001.I. A New Model for the Galactic Distribution of Free Electrons and its Fluctuations. *arXiv e-prints astro-ph/0207156* (2002).
40. Yao, J. M., Manchester, R. N. & Wang, N. Determination of the Sun's offset from the Galactic plane using pulsars. *Mon. Not. R. Astron. Soc.* **468**, 3289–3294 (2017).
41. Ransom, S. M. *New search techniques for binary pulsars*. Ph.D. thesis, Harvard University, Massachusetts (2001).
42. Wang, P. *et al.* FAST discovery of an extremely radio-faint millisecond pulsar from the Fermi-LAT unassociated source 3FGL J0318.1+0252. *Science China Physics, Mechanics, and Astronomy* **64**, 129562 (2021).
43. Astropy Collaboration *et al.* The Astropy Project: Building an Open-science Project and Status of the v2.0 Core Package. *Astron. J.* **156**, 123 (2018).
44. Pacheco, T. A., Diaz, M. P., Levenhagen, R. S. & Coelho, P. R. T. A Grid of Synthetic Spectra for Subdwarfs: Non-LTE Line-blanketed Atmosphere Models. *Astrophys. J. Supp.* **256**, 41 (2021).
45. Zhang, B. *et al.* Self-consistent Stellar Radial Velocities from LAMOST Medium-resolution Survey DR7. *Astrophys. J. Supp.* **256**, 14 (2021).
46. Zhang, B., Liu, C. & Deng, L.-C. Deriving the Stellar Labels of LAMOST Spectra with the Stellar LAbel Machine (SLAM). *Astrophys. J. Supp.* **246**, 9 (2020).
47. Fulton, B. J., Petigura, E. A., Blunt, S. & Sinukoff, E. RadVel: The Radial Velocity Modeling Toolkit. *PASP* **130**, 044504 (2018).
48. GRAVITY Collaboration *et al.* A geometric distance measurement to the Galactic center black hole with 0.3% uncertainty. *Astron. Astrophys.* **625**, L10 (2019).
49. Bland-Hawthorn, J. & Gerhard, O. The Galaxy in Context: Structural, Kinematic, and Integrated Properties. *ARA&A* **54**, 529–596 (2016).
50. Huang, Y. *et al.* Determination of the local standard of rest using the LSS-GAC DR1. *Mon. Not. R. Astron. Soc.* **449**, 162–174 (2015).
51. Zhou, Y., Li, X., Huang, Y. & Zhang, H. The Circular Velocity Curve of the Milky Way from 5-25 kpc Using Luminous Red Giant Branch Stars. *Astrophys. J.* **946**, 73 (2023).
52. Price-Whelan, A. M. Gala: A Python package for galactic dynamics. *The Journal of Open Source Software* **2**, 388 (2017).
53. Bovy, J. galpy: A python Library for Galactic Dynamics. *Astrophys. J. Supp.* **216**, 29 (2015).
54. Hubeny, I. & Lanz, T. Non-LTE Line-blanketed Model Atmospheres of Hot Stars. I. Hybrid Complete Linearization/Accelerated Lambda Iteration Method. *Astrophys. J.* **439**, 875 (1995).
55. Hubeny, I. & Lanz, T. TLUSTY User's Guide III: Operational Manual. *arXiv e-prints arXiv:1706.01937* (2017).
56. Lightkurve Collaboration *et al.* Lightkurve: Kepler and TESS time series analysis in Python. *Astrophysics Source Code Library* (2018).
57. Claret, A. *et al.* Gravity and limb-darkening coefficients for compact stars: DA, DB, and DBA eclipsing white dwarfs. *Astron. Astrophys.* **634**, A93 (2020).
58. Foreman-Mackey, D. *et al.* emcee: The MCMC Hammer. *Astrophysics Source Code Library, record ascl:1303.002* (2013).
59. Hurley, J. R., Pols, O. R. & Tout, C. A. Comprehensive analytic formulae for stellar evolution as a function of mass and metallicity. *Mon. Not. R. Astron. Soc.* **315**, 543–569 (2000).
60. Hurley, J. R., Tout, C. A. & Pols, O. R. Evolution of binary stars and the effect of tides on binary populations. *Mon. Not. R. Astron. Soc.* **329**, 897–928 (2002).
61. Miller, G. E. & Scalo, J. M. The Initial Mass Function and Stellar Birthrate in the Solar Neighborhood. *Astrophys. J. Supp.* **41**, 513 (1979).
62. Han, Z., Podsiadlowski, P. & Eggleton, P. P. The formation of bipolar planetary nebulae and close white dwarf binaries. *Mon. Not. R. Astron. Soc.* **272**, 800–820 (1995).
63. Ivanova, N. *et al.* Common envelope evolution: where we stand and how we can move forward. *A&A Rev.* **21**, 59 (2013).
64. Loveridge, A. J., van der Sluys, M. V. & Kalogera, V. Analytical Expressions for the Envelope Binding Energy of Giants as a Function of Basic Stellar Parameters. *Astrophys. J.* **743**, 49 (2011).
65. Zuo, Z.-Y. & Li, X.-D. On the common envelope efficiency. *Mon. Not. R. Astron. Soc.* **442**, 1980–1991 (2014).
66. Paxton, B. *et al.* Modules for Experiments in Stellar Astrophysics (MESA). *Astrophys. J. Supp.* **192**, 3 (2011).
67. Sen, K. *et al.* Detailed models of interacting short-period massive binary stars. *Astron. Astrophys.* **659**, A98 (2022).
68. Han, Z., Podsiadlowski, P., Maxted, P. F. L. & Marsh, T. R. The origin of subdwarf B stars - II. *Mon. Not. R. Astron. Soc.* **341**, 669–691 (2003).
69. Han, Z. & Chen, X. Envelope loss of RGB/AGB stars and the formation of hot subdwarfs. In *European Physical Journal Web of Conferences*, vol. 43 of *European Physical Journal Web of Conferences*, 01007 (2013).
70. Kupfer, T. *et al.* The First Ultracompact Roche Lobe-Filling Hot Subdwarf Binary. *Astrophys. J.* **891**, 45 (2020).
71. Geier, S. *et al.* The catalogue of radial velocity variable hot sub-luminous stars from the MUCHFUSS project. *Astron. Astrophys.* **577**, A26 (2015).
72. Astropy Collaboration *et al.* Astropy: A community Python package for astronomy. *Astron. Astrophys.* **558**, A33 (2013).
73. van der Walt, S., Colbert, S. C. & Varoquaux, G. The NumPy Array: A Structure for Efficient Numerical Computation. *Computing in Science and Engineering* **13**, 22–30 (2011).
74. Harris, C. R. *et al.* Array programming with NumPy. *Nature* **585**, 357–362 (2020).
75. Jones, E., Oliphant, T. & Peterson, P. SciPy: open source scientific tools for Python (2001).
76. Virtanen, P. *et al.* SciPy 1.0: Fundamental Algorithms for Scientific Computing in Python. *Nature Methods* **17**, 261–272 (2020).

Acknowledgements We acknowledge the staff of the XLT and Palomar observatories for assistance with the observations. We thank Jia-Lu Nie and Dr. Yu-Jiao Yang for Palomar remote observatories. We thank Prof. Xiao-Bing Zhang for discussions. This work is supported by the National Natural Science Foundation of China (NSFC) for grants No. 11988101, No. 11933004, No. 12288102, No.12125303, No. 12090040, and No. 12225304. This work is also supported by the National Key R&D Program of China grants No. 2019YFA0405500, No. 2021YFA1600400, and No. 2021YFA1600401, the China Manned Space Project with no. CMS-CSST-2021-A08 and CMS-CSST-2021-A10. Z.W.L. acknowledges support from NSFC grant No. 12103086 and the Yunnan Fundamental Research Projects (YFRP) grant Nos. 202201AU070234 and 202301AT070314. D.D.L. is supported by NSFC grant No. 12273105, the Youth Innovation Promotion Association CAS grant No. 2021058, the Western Light Project of CAS (No. XBZG-ZDSYS-202117), and the YFRP grants No. 202301AV070039, No. 202101AT070027 and No. 202101AW070047. Y.P.L. acknowledges support from NSFC grant no. 12173028. B.Z. acknowledges the support from NSFC under grant No.12203068. P.W. acknowledges support from the NSFC under grant No. U2031117, the Youth Innovation Promotion Association CAS (id. 2021055), CAS Project for Young Scientists in Basic Research grant No. YSBR-006 and the Cultivation Project for FAST Scientific Payoff and Research Achievement of CAMS-CAS. P.N. acknowledges support from the Grant Agency of the Czech Republic (GAČR 22-34467S). The Astronomical Institute in Ondřejov is supported by the project RVO:67985815. X.F.C. also acknowledges support from the NSFC for grants No. 12288102, No. 12125303. and No. 12090043, and the International Centre of Supernovae, Yunnan Key Laboratory (No. 202302AN360001), the Yunnan Fundamental Research Projects (grant Nos. 202201BC070003, 202001AW070007) and the “Yunnan Revitalization Talent Support Program” – Science & Technology Champion Project (No. 202305AB350003). J.F.L. acknowledges support the NSFC through grant Nos. of 11988101 and 11933004, and support from the New Cornerstone Science Foundation through the New Cornerstone Investigator Program and the XPLOER PRIZE.

Guoshoujing Telescope (the Large Sky Area Multi-Object Fiber Spectroscopic Telescope, LAMOST) is a National Major Scientific Project built by the Chinese Academy of Sciences. The National Development and Reform Commission has provided funding for the project. LAMOST is operated and managed by the National Astronomical Observatories, Chinese Academy of Sciences.

We used data from the European Space Agency mission Gaia (<http://www.cosmos.esa.int/gaia>), processed by the Gaia Data Processing and Analysis Consortium (DPAC; see <http://www.cosmos.esa.int/web/gaia/dpac/consortium>). We also used the data from the SDSS survey.

This paper includes data collected by the TESS mission. Funding for the TESS mission is provided by the NASA Explorer Program. This work presents results from the European Space Agency (ESA) space mission Gaia. Gaia data are being processed by the Gaia Data Processing and Analysis Consortium (DPAC). Funding for the DPAC is provided by national institutions, in particular the institutions participating in the Gaia Multi Lateral Agreement (MLA).

This research has used the services of www.Astroserver.org under reference OL4CLY.

Author Contributions C.Q.L. discovered this system and led the follow-up observations, wrote parts of the manuscript; J.L. led the analysis of the light curve and spectra, wrote parts of the manuscript; C.J.Z. led the analysis of the light curve modelling and SED fitting, wrote parts of the manuscript; D.D.L. led the binary population synthesis simulation; Z.W.L. performed the MESA numerical simulations to investigate the life of this system; Y.P.L. assisted with the determinations of stellar parameters of the hot subdwarf; P.N. determined the stellar parameters of the hot subdwarf using the XT_{GRID} tool; B.Z. assisted with the data reduction of P200; J.P.X. helped the remote observations; B.W. joined the discussions and contributed to the re-

visions of the text; S.W. helped the remote observations; Y.B. helped the remote observations; Q.Z.L. performed the kinematic analysis of this system; P.W. performed the data reduction and analysis of FAST observations; Z.W.H. helped the interpretation of the results; J.F.L. contributed to the interpretation of the results and revised the text; Y.H. wrote the manuscript and partly led the project; X.F.C. led the interpretation of the results and revised the text; C.L. led the project, organized the observations and revised the text.

Competing interests statement The authors declare no competing interests.

Author Information Correspondence and requests for materials should be addressed to Yang Huang, Xuefei Chen and Chao Liu.